J. Fluid Mech. (2003), *vol.* 484, *pp.* 223–253.
DOI: 10.1017/S0022112003004257 Printed in the United Kingdom

Large-eddy simulations of ducts with a free surface

By RICCARDO BROGLIA[1], ANDREA PASCARELLI[1] AND UGO PIOMELLI[2]

[1]INSEAN, Via di Vallerano 139, 00128 Roma, Italy

[2]Department of Mechanical Engineering, University of Maryland, College Park, MD 20742, USA

(Received 27 March 2002 and in revised form 7 January 2003)

This work studies the momentum and energy transport mechanisms in the corner between a free surface and a solid wall. We perform large-eddy simulations of the incompressible fully developed turbulent flow in a square duct bounded above by a free-slip wall, for Reynolds numbers based on the mean friction velocity and the duct width equal to 360, 600 and 1000. The flow in the corner is strongly affected by the advection due to two counter-rotating secondary-flow regions present immediately below the free surface. Because of the convection of the inner eddy, as the free surface is approached, the friction velocity on the sidewall first decreases, then increases again. A similar behaviour is observed for the surface-parallel Reynolds-stress components, which first decrease and then increase again very close to the surface. The budgets of the Reynolds stresses show a strong reduction of all terms of the dissipation tensor in both the inner and outer near-corner regions. They exhibit a reduction in both production and dissipation towards the free surface. Very close to the solid boundary, within 15–20 viscous lengths of the sidewall, the turbulent kinetic energy production and the surface-parallel fluctuations rebound in the thin layer adjacent to the free surface. The Reynolds-stress anisotropy appears to be the main factor in the generation of the mean secondary flow. The multi-layer structure of the boundary layer near the free surface is also discussed.

1. Introduction

Mixed-boundary corner flows occur at the juncture of a no-slip wall and a free surface. They can be found in a variety of practical applications: the flow around hulls of ships is perhaps the most common example of this configuration, which also occurs on the sidewall boundary of an open channel or of a partially filled container, and in rivers. An important feature of these flows is the interaction of wall turbulence with a free surface. When turbulence interacts with either a free surface or a solid wall, it becomes highly anisotropic. The character of the anisotropy, however, is substantially different in the two cases. A free surface cannot support mean shear, and restricts motion in the direction normal to the surface only, while a solid wall forces all the velocity components to vanish at the boundary. The no-slip condition at a solid wall makes turbulence production and dissipation significant there, whereas at a free surface turbulence production is negligible and the dissipation rate is smaller than in the bulk of the flow because of the vanishing of the velocity gradients. Near a mixed-boundary corner, the interaction of the eddies generated by these different

mechanisms creates additional physical complexities (compared either with the free surface or the solid wall alone) that affect the transport of mass, momentum and energy. In order to predict the flow fields in the applications mentioned above, better understanding of their physics is required.

The characteristics of the flow near a solid flat surface are well known and will not be discussed here. Descriptions of the statistical aspects of the flow and of the turbulent eddies can be found in many textbooks and reviews (see, e.g. Pope 2000; Robinson 1991). The structure of the wall turbulence, however, is significantly altered in the corner between two solid walls, where the anisotropy of the Reynolds stresses generates turbulence-driven secondary flows in the plane perpendicular to the streamwise direction, commonly referred to as 'secondary flows of Prandtl's second kind'. In straight square ducts, the secondary flow is directed from the centre of the duct toward the corners along the corner bisectors. Although the magnitude of these secondary velocities is extremely small (of the order of 2–3% of the bulk streamwise velocity), the distortion of the axial flow can alter the distribution of the friction coefficient (and thus the mean flow).

Because of the complex physics coupled with a simple geometry, these flows have been studied extensively, both experimentally and numerically. While the experiments (Launder & Ying 1972; Melling & Whitelaw 1976; Gessner, Po & Emery 1979) were the first to quantify the mean flow, numerical calculations (Madabhushi & Vanka 1991; Gavrilakis 1992; Huser & Biringen 1993; Huser, Biringen & Hatay 1994; Su & Friedrich 1994) have been instrumental in addressing questions related to turbulent kinetic energy (TKE) production and transfer, as well as to the modifications to the turbulence structure in these configurations. Huser *et al.* (1994) investigated the details of the Reynolds stress budgets and performed quadrant analysis to examine the dominant structures which give rise to the generation of secondary flows. They observed that the dominant ejections contain two streamwise counter-rotating vortices.

Modifications to the turbulence structure occur also when turbulence interacts with a free surface, where the relative velocity between the fluid and the surface interface vanishes, the tangential stresses are zero, and the normal stress must balance the ambient pressure. In addition, in the free-surface case, the boundary can deform. If the free surface can be considered flat, the tangential vorticity vanishes at the free surface but not the component normal to the surface, while in the case of a shear-free deformed free surface, the vorticity at the free surface is non-zero and the surface acquires a solid-body rotation. The non-dimensional groups that appear in these flows are the Reynolds number, the Froude number and the Weber number, defined as $Fr = u_r/\sqrt{gl_r}$ and $We = \rho l_r u_r^2/\sigma_s$, respectively, where g is the acceleration due to gravity, σ_s the surface tension, and u_r and l_r are a reference velocity and length. The Froude number, which is related to the deformation of the free surface, is the most important one for the present study; low Froude numbers correspond to negligible free-surface deformations.

Perhaps the main feature of the interaction of turbulence with the free surface is the modification of the inter-component energy transfer, which has been observed by virtually all the workers who have examined this problem. In the boundary layer adjacent to the free surface, the fluctuations parallel to the surface are essentially unaltered, while the Reynolds-stress component normal to the surface is redistributed into surface-parallel components, which increase with decreasing distance from the free surface. In the case of a free-slip flat surface, a picture of the vortex/surface interactions on the dynamics of turbulence under the free surface emerges from the

direct numerical simulation (DNS) studies of Perot & Moin (1995), Walker, Leighton & Garza-Rios (1996) and Nagaosa (1999).

A complete discussion of the 'multi-layer structure' of free-surface viscous flow is not appropriate here (for a more complete review see Shen *et al.* 1999), but a few significant results should be described. As shown originally by Hunt & Graham (1978), a two-layer model can describe the interaction between a shear-free boundary and turbulence. The layer through which the kinematic boundary condition is felt is defined as the 'blockage' or 'source' layer, whereas the thin zone near the free surface due to the viscous dynamic conditions is called the 'surface' layer. The blockage layer, which is due to the zero normal-velocity condition at the free surface, obtains for any flow with a boundary constraining the normal motion; redistribution of turbulent intensities takes place here. In the surface layer, the velocity derivatives are highly anisotropic, and the values of the surface-parallel vorticity change from 'outer' values to smaller values induced by the boundary conditions. The important scales in the source layer are the integral scales of the turbulence far below the boundary, while the viscous layer is characterized by velocity and length scales determined by its own internal dynamics. When a turbulent shear flow interacts with a free surface, additional complexities appear. Further investigations of the surface layer can be found in the work of Anthony & Willmarth (1992) and Walker (1997), who associated the origin of the current to the near-surface turbulent-stress anisotropy. When the surface deforms, the Reynolds-stress anisotropy is smaller and the free-surface fluctuations make a significant contribution (Hong & Walker 2000).

Turbulent channel flows bounded by a rigid wall below and an open free surface above have been investigated experimentally (Nakagawa & Nezu 1981; Komori *et al.* 1982; Nezu & Rodi 1986) and numerically (Lam & Banerjee 1992; Leighton *et al.* 1981; Handler *et al.* 1993; Pan & Banerjee 1995). In this configuration, the turbulence produced near the solid wall owing to the high shear can be convected to the surface and interact with it, a situation that occurs, for instance, in rivers. While the investigations cited above approximated the free surface as flat, other studies employed more realistic approaches (e.g. Komori *et al.* 1993; Borue, Orszag & Staroselsky 1995; Tsai 1998). However, in the cases considered, the interfacial deformations and the normal velocity at the free surface remained extremely small, so that no significant deviations from the flat-surface case were observed.

In all the free-surface/turbulence interaction studies discussed so far, the flow is homogeneous in the spanwise (surface-parallel) direction. In this case, several workers have inferred the quasi-two-dimensionalization of turbulence structure near the free surface (Sarpkaya & Suthon 1991; Sarpkaya & Neubert 1994; Pan & Banerjee 1995; Kumar, Gupta & Banerjee 1998). Turbulent shear flows bounded by a vertical wall and a horizontal free surface may differ significantly from those. In the region close to the walls or in other situations where turbulence is being generated, for instance, the eddy structure will certainly be markedly three-dimensional, even near a free surface. The existence of mean secondary flows in the corner (similar to those that occur in the closed ducts) adds complexity to the problem. Studies of turbulent flows in the corner formed by a vertical solid wall and a free surface have been performed, among others, by Grega *et al.* (1995), Longo, Huang & Stern (1998), Sreedhar & Stern (1998), Hsu *et al.* (2000) and Grega, Hsu & Wei (2002).

Grega *et al.* (1995) carried out numerical simulations in conjuction with experimental flow visualization and single-component laser-Doppler anemometry (LDA) velocity measurements. The Reynolds number of the experimental investigation was $Re_\theta = 1150$ (based on the momentum thickness θ), while the numerical

simulation was performed at $Re_\theta = 220$. In their work, the presence of the mean inner and outer secondary flow regions was highlighted. While the inner secondary region has a parallel in the flow in a corner formed by two solid walls, the outer secondary flow region does not have an analogue in the wall-bounded corner flow. The inner secondary vortex convects fluid from the free surface toward the corner, surrounded by the outer flow, which convects flow from the sidewall to the free surface. In Grega *et al.* (1995), the inner secondary flow was very weak, and could not be observed by flow visualization; it was, however, resolved in the computations. Longo *et al.* (1998) examined the flow in the corner formed by a towed surface-piercing plate and a free surface at rest. Three-component laser-Doppler velocimetry (LDV) measurements for both boundary layer and wake were also used to obtain scaling properties for the anisotropy of the normal Reynolds stresses. However, in this case also, the marginal measurement resolution did not permit visualization of the inner secondary vortex motion. Sreedhar & Stern (1998) carried out large-eddy simulations (LES) of compressible temporally developing solid/solid and solid/rigid-lid corner flows. In these simulations, in which the inner secondary flow was resolved, the TKE increased near the rigid-lid boundary and a redistribution of energy from the surface normal components to the other two was also observed in this region. There is some controversy on this issue, since Longo *et al.* (1998) and Sreedhar & Stern (1998) predict an increase of mean-square streamwise velocity fluctuations as the distance from the free surface decreases, while Grega *et al.* (1995), in their experiments, measure an increase in this quantity. Similar discrepancies are found in the behaviour of the anisotropy-tensor profiles. As an extension of the work of Grega *et al.* (1995), Hsu *et al.* (2000) studied the TKE transport mechanisms in the mixed-boundary corner using high-resolution digital particle image velocimetry (DPIV) and LDV measurements. They found that both TKE production and dissipation are dramatically reduced close the free surface.

Some of the conclusions of Longo *et al.* (1998) and Sreedhar & Stern (1998) also appear to be in conflict with the results obtained by the follow-up experimental study of the same problem by Hsu *et al.* (2000), suggesting that the dynamics of boundary-layer/free-surface juncture have not been perfectly elucidated. Furthermore, certain issues were not fully addressed owing to limitations of experimental investigations, for example the resolution of the flow very near the free surface. The origin of the inner secondary flow in the context of vorticity transport, the role played by the diverging surface current found when studying jets, wakes or boundary layers parallel to a free surface (Walker 1997), the vortex structures in a turbulent mixed-boundary corner, are examples of the questions not yet conclusively investigated. Many of the discrepancies are probably due to different set-ups in the different studies, as also mentioned by Grega *et al.* (2002). High-resolution DPIV measurements made in the cross-stream plane by Grega *et al.* (2002) using the same experimental apparatus as two earlier works by the authors, pointed out that there is an, as yet, undetermined source of streamwise vorticity particularly in the outer secondary flow region close to the free surface.

The objective of this work is to address some of the issues mentioned above and resolve some of the discrepancies between previous studies by performing LES of the flow inside a square duct bounded by a gas–liquid interface at the top. In particular, we will computationally provide a complete picture of the secondary flows. The features of these flows will be related to the presence of a free-surface current, and *inter alia* the effects on turbulence statistics of the peculiar boundary-layer structure will be investigated. After having demonstrated the accuracy of the numerical tool,

we will study the inner secondary flow in the context of the streamwise budget of momentum equation and vorticity transport; then, we will attempt to provide a detailed description of the turbulent energy transport mechanisms in the mixed-boundary corner. The use of LES (rather than DNS) allows us to perform calculations at three Reynolds numbers, $Re_\tau = 360$, 600 and 1000 (based on the mean friction velocity and the duct width).

The paper is organized as follow: in the next section, the problem formulation, numerical method and subgrid-scale model used are briefly described. Then, the results of a closed-duct calculation will be presented to validate the code. Discussion of the mean flow, Reynolds stress and vorticity statistics will follow. Finally, some conclusions will be drawn in the last section.

2. Problem formulation

2.1. *Governing equations and numerical method*

The governing equations for LES are obtained by the application of a spatial filter to the Navier–Stokes equations to separate the effects of the (large) resolved scale from the (small) subgrid-scale (SGS) eddies; in the case of an incompressible viscous flow in presence of body forces, they can be written in the following form:

$$\frac{\partial \overline{u}_i}{\partial t} + \frac{\partial}{\partial x_j}(\overline{u}_j \overline{u}_i) = -\frac{\partial \overline{p}}{\partial x_i} + \frac{1}{Re_\tau}\nabla^2 \overline{u}_i - \frac{\partial \tau_{ji}}{\partial x_j} + f_i, \quad \frac{\partial \overline{u}_j}{\partial x_j} = 0, \tag{2.1}$$

where the overbar denotes filtered variables and the effect of the subgrid scales appears through the SGS stresses $\tau_{ij} = \overline{u_i u_j} - \overline{u}_i \overline{u}_j$; u_j is the fluid velocity component in the j-direction and p is the pressure divided by the constant density. Equations (2.1) are non-dimensionalized using the mean friction velocity, u_τ, and the duct width, D, as characteristic velocity and length scales, respectively. Thus, the Reynolds number is defined as $Re_\tau = u_\tau D/\nu$, where ν is the kinematic viscosity. The flow is driven by a constant body force per unit mass, f_1. Periodic boundary conditions are used in the streamwise directions and no-slip boundary conditions are imposed on walls. The boundary conditions enforced on the top surface of the computational domain are either the no-slip conditions

$$u = 0, \quad v = 0, \quad w = 0, \tag{2.2}$$

or the no-stress boundary conditions

$$\frac{\partial u}{\partial z} = 0, \quad \frac{\partial v}{\partial z} = 0, \quad w = 0. \tag{2.3}$$

Despite the limitations of these assumptions, previous numerical studies have shown that a rigid free-slip wall approximation allows us to predict many of the phenomena seen in experiments with waveless interfaces (Lam & Banerjee 1992; Leighton *et al.* 1981; Handler *et al.* 1993; Pan & Banerjee 1995).

In the present work, the SGS stresses τ_{ij} are parameterized by an eddy-viscosity model of the form:

$$\tau_{ij} - \tfrac{1}{3}\delta_{ij}\tau_{kk} = -2\nu_T \overline{S}_{ij} = -2C\Delta^2 |\overline{S}| \overline{S}_{ij}, \tag{2.4}$$

where δ_{ij} is Kronecker's delta, $|\overline{S}| = (2\overline{S}_{ij}\overline{S}_{ij})^{1/2}$ is the magnitude of the large-scale strain-rate tensor $\overline{S}_{ij} = (\partial \overline{u}_i/\partial x_j + \partial \overline{u}_j/\partial x_i)/2$, and $\Delta = 2(\Delta x \Delta y \Delta z)^{1/3}$ is the filter width. Closure of the SGS stresses τ_{ij} is obtained through specification of the

model coefficient C appearing in (2.4). In the present work, the dynamic procedure proposed by Germano *et al.* (1991) and Lilly (1992) is used to determine the eddy-viscosity coefficient C. The constant C is averaged along the homogeneous streamwise direction; this type of averaging is effective in removing spurious fluctuations of C which tend to destabilize the calculations, and has been used in several calculations of turbulent flows that are homogeneous in one direction only (Akselvoll & Moin 1996; Mittal & Moin 1997), with accurate results. The sum of the laminar and eddy viscosity is set to zero wherever it becomes negative.

The numerical approach employed for the solution of (2.1) is the fractional step method (Chorin 1967; Kim & Moin 1985). The time-advancement for the intermediate advection-diffusion step is performed in a semi-implicit fashion with a two-substep second-order accurate Runge–Kutta algorithm. This is followed by the pressure-correction step, which enforces the divergence-free condition; the Poisson equation for the pressure-like function is solved once per time step. All the spatial derivatives are approximated using a second-order-accurate central discretization on a non-uniform collocated grid. Solution of the Poisson equation is obtained by means of a successively over-relaxed Gauss–Seidel method; a multigrid algorithm of a correction-scheme type is used to accelerate the convergence toward the solution. Implicit treatment of the diffusive terms allows a larger time step, which is only limited by the explicit treatment of the advective and SGS terms. The overall accuracy of the method is second order in time and space.

Parallelization of the code is achieved by an effective domain decomposition technique; the domain is divided into a number of subdomains along the streamwise direction. Communications between processors are made by using the message-passing programming and the *send*, *receive* and *reduce* statements of the message-passing library Message-Passing Interface (MPI). This algorithm is described in detail in Broglia, Di Mascio & Muscari (1999).

2.2. *Geometry and grid parameters*

The Navier–Stokes equations are solved numerically in a rectangular domain of size $2\pi D \times D \times D$ in the x-, y- and z-directions, respectively. The streamwise length of the domain was chosen based on the two-point velocity correlations computed by Huser & Biringen (1993) to ensure that the domain is large enough to contain the longest structure present in the flow.

The physical domain is discretized using between 4.7×10^5 grid points for the low-Reynolds-number simulation, and 5.6×10^6 grid points for the high-Reynolds-number one. All the discretizations are uniform in the streamwise (x) direction, whereas in the spanwise and normal directions (y and z, respectively) points are clustered towards the walls; in particular, for all the simulations, the first point close to the wall is placed at y^+ or $z^+ = 0.5$ and at least 13 points are in the near-wall region (y^+ or $z^+ < 10$). Points are also clustered toward the slip wall, with a minimum grid spacing of about 1.5 wall units for the high Reynolds numbers and 0.5 for the lowest one. The problem geometry is sketched in figure 1, and the mesh characteristics are given in table 1.

The equations were integrated in time until a statistical steady state was reached (the steady state was determined by monitoring the time history of the total wall shear stress). After that, data for the statistics were collected for several large-eddy turnover times (LETOTs) D/u_τ. Streamwise homogeneity and symmetry about the plane $y = 0.5D$ were used to increase the sample size. The sampling interval for each case (also in LETOTs) is reported in table 2. The relevant non-dimensional parameters

Simulation	$nx \times ny \times nz$	Δx^+	Δy^+ min–max	Δz^+ min–max	Points in y^+ or $z^+ < 10$
Closed duct, $Re_\tau = 360$	$50 \times 97 \times 97$	48.1	0.5–8.1	0.5–8.1	13
Closed duct, $Re_\tau = 600$	$82 \times 129 \times 129$	47.7	0.5–10.7	0.5–10.7	14
Open duct, $Re_\tau = 360$	$50 \times 97 \times 97$	48.1	0.5–8.1	0.5–8.1	13
Open duct, $Re_\tau = 600$	$82 \times 129 \times 129$	47.7	0.5–10.7	0.5–10.7	14
Open duct, $Re_\tau = 1000$	$144 \times 197 \times 197$	43.9	0.5–11.6	0.5–11.9	15

TABLE 1. Grid characteristics.

Simulation	Sampling time Δt	U_b	U_c	Computed u_τ	Re_b
Duct $Re_\tau = 360$	16.19	15.35	19.30	1.0012	5526
Duct $Re_\tau = 600$	9.42	16.54	20.27	1.0055	9924
Open duct $Re_\tau = 360$	12.77	15.48	18.39	1.0006	5571
Open duct $Re_\tau = 600$	13.08	16.41	19.12	1.0024	9844
Open duct $Re_\tau = 1000$	5.03	17.13	20.12	0.9953	17 130

TABLE 2. Averaging and global flow characteristics. U_c is the maximum velocity in the duct.

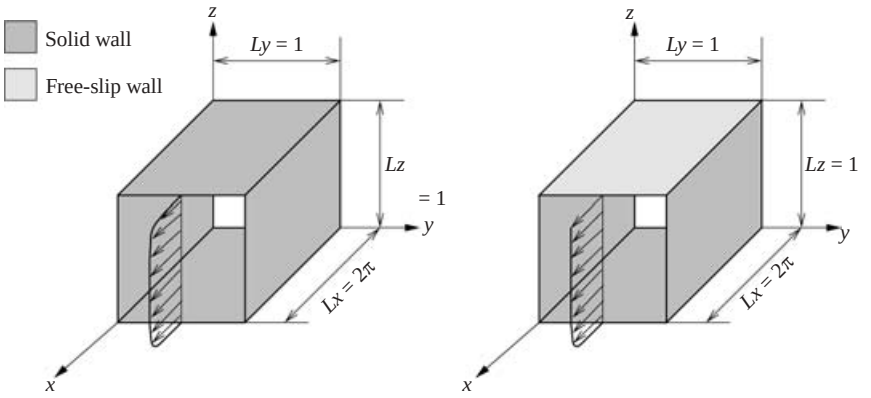

FIGURE 1. Sketch of the problems.

are the Reynolds number based on the friction velocity u_τ and the duct width D, $Re_\tau = u_\tau D/\nu$, and the bulk Reynolds number defined using the bulk (area-averaged) streamwise velocity U_b, $Re_b = U_b D/\nu$. In table 2, the Reynolds numbers and some global results of the present simulations are shown. The value of u_τ obtained from the calculations is within 0.5% of the nominal value $u_\tau = 1$. This difference supplies an estimate of the sampling error for the first- and second-order statistics, which was, respectively, 0.5% and 1%.

In the following discussions, the angular brackets, $\langle\cdot\rangle$, denote an average over time and the homogeneous direction, whereas a double prime denotes fluctuation with respect to mean resolved quantity, $q'' = \overline{q} - \langle\overline{q}\rangle$; thus, the resolved quantities are decomposed into mean values and resolved fluctuations:

$$\overline{u}_i = \langle\overline{u}_i\rangle + u_i'', \qquad \overline{p} = \langle\overline{p}\rangle + p'', \qquad \tau_{ij} = \langle\tau_{ij}\rangle + \tau_{ij}''. \tag{2.5}$$

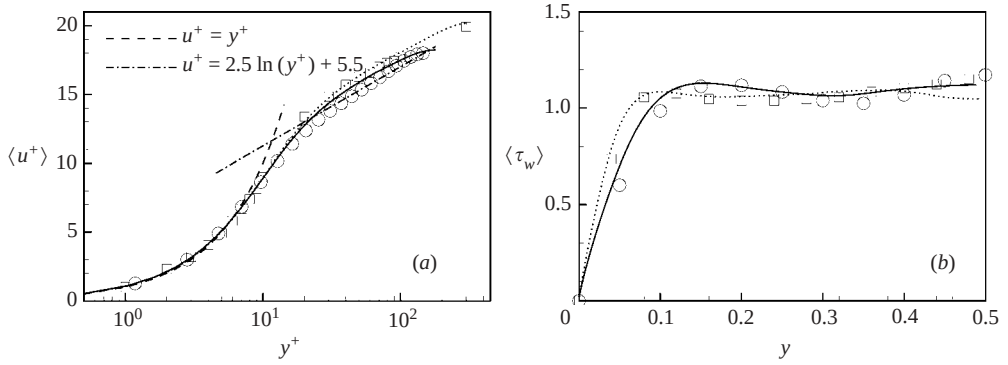

FIGURE 2. Duct flow. (*a*) Mean streamwise velocity profiles along the wall bisector; (*b*) wall stress distribution along the sidewall. ——, $Re_\tau = 360$; · · · · · ·, $Re_\tau = 600$; ○, DNS at $Re_\tau = 300$ (Gavrilakis 1992); □, DNS at $Re_\tau = 600$ (Huser & Biringen 1993).

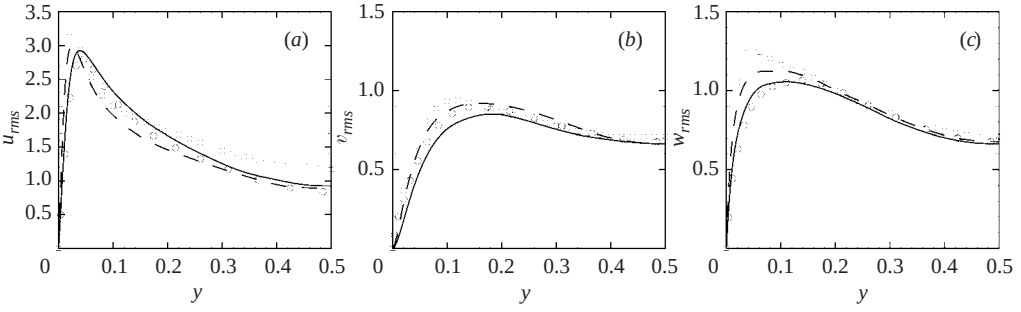

FIGURE 3. Duct flow. Root mean square velocity fluctuations along the wall bisector. (*a*) u; (*b*) v; (*c*) w. ——, $Re_\tau = 360$; – – –, $Re_\tau = 600$; ○, DNS at $Re_\tau = 300$ (Gavrilakis 1992); □, DNS at $Re_\tau = 600$ (Huser & Biringen 1993).

Thus, the averaged resolved velocity and turbulent stresses are denoted by $\langle \overline{u}_i \rangle$ and $\langle u_i'' u_j'' \rangle$, respectively.

3. Results and discussion

3.1. *Validation: closed duct flow*

To determine the accuracy of the present numerical method in configurations similar to the open duct, LES of fully developed turbulent flow in a closed square duct were performed and compared with the available DNS data. The current LES solutions at $Re_\tau = 360$ and 600 are compared with low-Reynolds-number DNS solution by Gavrilakis (1992) at $Re_\tau = 300$ ($Re_b = 4410$) and with those by Huser & Biringen (1993) at $Re_\tau = 600$ ($Re_b = 10\,320$).

Mean turbulent statistics are shown in figures 2 and 3. Here and in the following, unless otherwise stated, all quantities are normalized using the mean u_τ and D. The agreement with the DNS data is good. In particular, the overshoot in the logarithmic layer (figure 2*a*) observed in the DNS is captured quite well. The main topological features of the flow, such as the secondary vortices often observed in the corner region, are also captured well. Gavrilakis (1992) performed a DNS using a second-order finite difference on a staggered grid with up to 16.1×10^6 grid points ($768 \times 127 \times 127$) and a

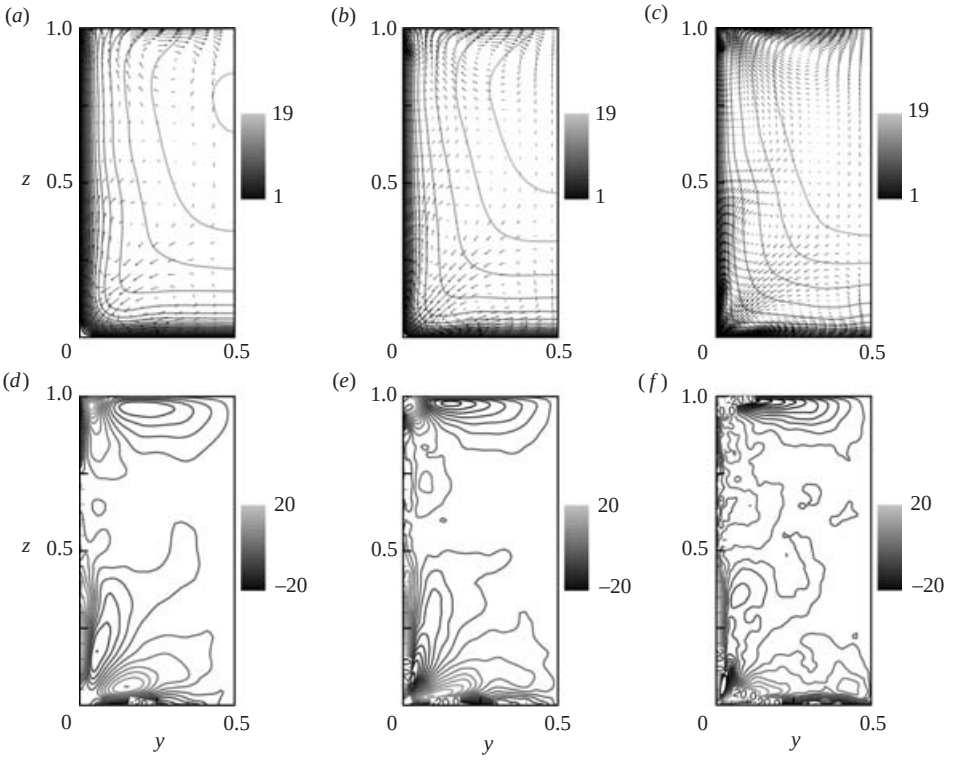

FIGURE 4. Open duct flow. (*a*)–(*c*) Mean streamwise velocity contours and secondary velocity vectors. (*d*)–(*f*) Vorticity contours. (*a*), (*d*) $Re_\tau = 360$; (*b*), (*e*) $Re_\tau = 600$; (*c*), (*f*) $Re_\tau = 1000$.

box length of $l_x = 10\pi$. Our calculation uses approximately one fifth of the resolution of this DNS (470,450 points are used to discretize a domain that is one fifth the length of that of Gavrilakis 1992). Our grid resolution, on the other hand, is comparable to that of the DNS by Huser & Biringen (1993), which used $96 \times 101 \times 101$ grid points with a spectral/high-order finite-difference scheme and a time-splitting integration method.

3.2. *Open duct: mean velocity*

Figure 4 shows mean streamwise-velocity contours and cross-stream velocity vectors in the cross-stream (y, z)-plane for the three Reynolds numbers considered here. In the figures, the free surface is at the top, and only half of the domain is shown. In the lower corner, the flow is very similar to that observed in closed square ducts: a turbulence-driven secondary flow, consisting of a streamwise counter-rotating vortex pair deforms the isotachs by convecting high-momentum fluid from the central region of the duct towards the corner region along the corner bisector. Contours of the resolved mean streamwise vorticity $\langle\omega_x\rangle = \partial\langle\overline{w}\rangle/\partial y - \partial\langle\overline{v}\rangle/\partial z$ show positive and negative extrema at the vertical and horizontal walls because of the no-slip conditions. In the centre of the larger flow-cells the vorticity attains extreme values locally. In the upper corner, on the other hand, the effects of the free-shear surface become important. The main feature of the flow field near the mixed corner is the existence of an 'inner' and an 'outer' mean secondary flow, as observed in the unbounded corner flow studied by Grega *et al.* (1995). The 'inner secondary region' at the mixed corner consists of a

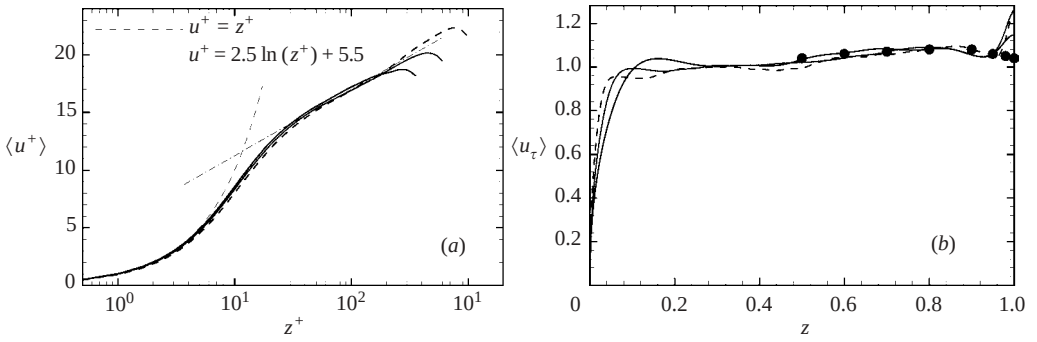

FIGURE 5. Open duct flow. (*a*) Mean streamwise-velocity profiles in wall units along the bottom-wall bisector; (*b*) friction velocity distributions along the sidewall. ——, $Re_\tau = 360$; ·····, $Re_\tau = 600$; – – –, $Re_\tau = 1000$; ●, u_τ obtained at $Re_\tau = 600$ from the Clauser plot.

weak vortex that convects momentum towards the corner itself, along the free-slip boundary, whereas the 'outer secondary vortex' is responsible for transport of low-speed momentum from the sidewall boundary-layer, towards the free surface. The scale and strength of the outer secondary vortex are larger than those of the other vortices appearing in the cross-plane view. The maximum value of the secondary velocity is about 3% of the streamwise velocity, slightly greater than that observed in the closed duct case. Furthermore, the contours of mean streamwise vorticity show a direct correspondence with the secondary flow. A small increase of the secondary-flow intensity with the Reynolds number is observable. The flow behaviour near the sidewall in the region around $z = 0.5$ shows a transition between the corner and the free-surface behaviour, characterized by a weaker counter-clockwise vortical motion. This vortex is prevented from growing to dimensions and strength comparable to the corner eddy by the presence of the two surface vortical structures, but its effects on the flow field are important. In particular, it thickens the wall layer in this region, affecting the wall stress distribution and the momentum transport. Such a vortical region was not observed by Grega *et al.* (1995), suggesting that is driven by the anisotropic turbulence generated by the bottom no-slip wall.

In figure 5(*a*), the mean streamwise-velocity profiles in logarithmic scale along the bottom-wall bisector ($y = 0.5$) are presented for the three Reynolds numbers considered. They satisfy the logarithmic law very well, and maintain the log-law behaviour until very close to the free surface. Compared with the closed-duct case, we do not observe the overshoot of the logarithmic layer intercept. Since the grid resolution for the closed- and open-duct calculations was the same, this can be interpreted as a results of slightly weaker turbulence production near the walls away from the duct corners, compared with the companion closed-duct flow. The mean velocity profiles exhibit a maximum near the free surface. In the region $0.8 < z/D < 1$ a zone of negative mean shear $\partial\langle\overline{u}\rangle/\partial z$ is observed (see figure 6), owing to the augmentation of the vertical descending convective transport caused by the outer secondary flow as the free surface is approached. The centre of the duct is the merging point of two opposite diverging currents generated at the sidewalls (Walker 1997). As reported in Shen, Triantafyllou & Yue (2000) for an unbounded shear flow, this is a first indicator of the boundary-layer structure near a free surface, whose maximum and minimum mark the ends of the two layers at the interface. Secondary flows clearly appear to have a significant effect on the region where these events

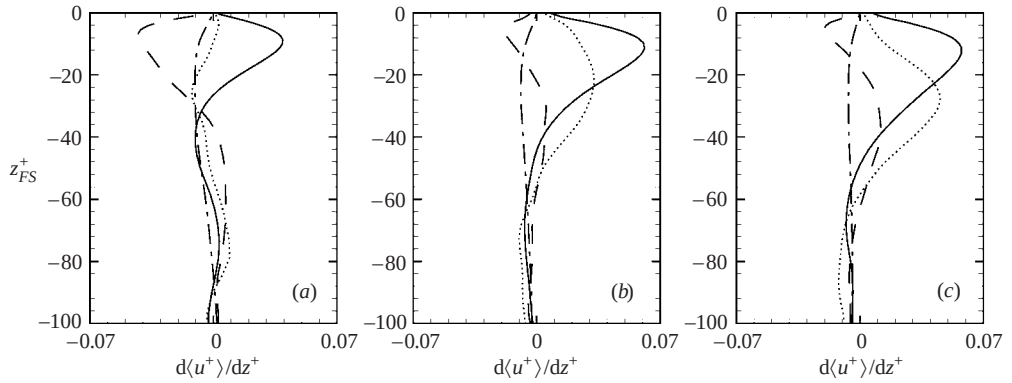

FIGURE 6. Open duct flow. Mean shear profiles normalized with u_τ^2/ν. z^+_{FS} is the distance from the free surface in wall units (the reference u_τ is used in this normalization). (*a*) $Re_\tau = 360$, (*b*) $Re_\tau = 600$, (*c*) $Re_\tau = 1000$. ——, $y^+ = 3$; · · · · · ·, $y^+ = 15$; – – –, $y^+ = 30$; —·—, $y^+ = Re_\tau/2$.

occur. Note that around the demarcation between the inner and outer secondary region ($y+ \sim 40$) a behaviour similar to that observed in shear-free unbounded flow is recovered, and that the size of the surface layer exhibits little Reynolds-number dependence.

In figure 5(*b*), the distributions of the mean friction velocity along the sidewall are shown. Grega *et al.* (1995) and Hsu *et al.* (2000) reported experimental data that show a thickening at the free-surface edge of the turbulent boundary layer on the vertical wall as a result of the free-surface current. Consistent with these results, the friction velocity from the present computations decreases as the free surface is approached. The present computations, however, also show an increase of u_τ very near the surface, again due to the inflow from the inner secondary cell, which convects high-speed momentum toward the sidewall at the free surface. This result is consistent with the numerical results presented in Grega *et al.* (1995) and indicates a reduction of the boundary-layer thickness in the vicinity of the free surface, which was not observed experimentally. Two causes can be the origin of the discrepancy between numerical and experimental data. One is the use of the $Fr = 0$ approximation, which is least accurate in the corner region. However, the experiments of Grega *et al.* (1995) and Hsu *et al.* (2000) were conducted at a low reference Froude number, so that waves and surface deformations are not expected to have a significant effect on the interaction of the free surface with the turbulence-driven secondary flows developed near the corner. The second, and perhaps most significant, factor relates to the method used in the experimental studies to determine the skin friction. Friction velocities were determined experimentally from the mean streamwise-velocity data measured at two different distances from the surface (60 and 5080 viscous lengths below the free surface, the latter profile corresponding to the tunnel centre). From each individual mean velocity profile, u_τ and the wall location were determined by fitting to the Clauser plot for a canonical turbulent boundary layer. In the corner region, however, the flow deviates significantly from the standard logarithmic behaviour. In figure 7, the velocity profiles and distances from the wall are normalized using the local value of u_τ. Near the free surface, the slope of the logarithmic region is significantly lower; here, friction velocities determined using the Clauser plot are not accurate. This is shown in figure 5(*b*) in which the solid dots represent the friction velocity calculated by requiring that the velocity profile satisfy the logarithmic region at $y^+ = 100$. Note

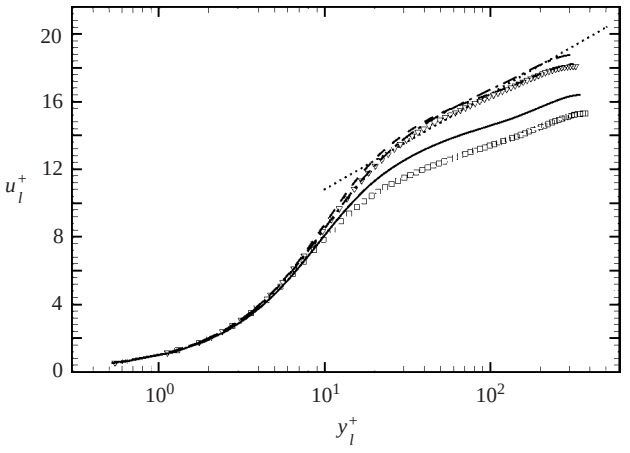

FIGURE 7. Open duct flow, $Re_\tau = 600$. Mean streamwise-velocity profiles in wall units for different distances from the free surface: □, $z = 1$; ——, $z = 0.98$; – – –, $z = 0.95$; ▽, $z = 0.8$; —·—, $z = 0.6$.

further that Stern *et al.* (1995) observe a secondary flow near the free-surface edge of a turbulent boundary layer on a vertical wall. The rotation of the secondary flow was such that the boundary layer was thinner as the free surface was approached. The secondary flow was explained in terms of the anisotropy in the Reynolds stresses. Increasing the Reynolds number results in a thickening of the sublayer on the lower wall, but has very little effect on the region close to the free surface.

3.3. *Open duct: Reynolds stresses*

Figure 8 shows the cross-stream spatial distribution of the Reynolds stresses in the $Re_\tau = 600$ case. In the present simulations, the SGS stresses are an order of magnitude smaller than the resolved ones (at least away from the walls), and the large-scale quantities shown in the following represent the contribution from most of the significant turbulent motions. Near the upper corner, the normal Reynolds stresses distributions are significantly different from the lower corner region. The streamwise normal stress $\langle u''u'' \rangle$ is nearly two-dimensional along most of the sidewall, and begins to decrease only very near the free surface; in the lower corner, by comparison, the distribution of $\langle u''u'' \rangle$ begins to be affected by the bottom wall at $z \simeq 0.2$. The other two normal components are more three-dimensional, affected both by the solid surface on the bottom and the free surface on top. At the free surface the w'' fluctuations vanish, and $\langle w''w'' \rangle = \langle u''w'' \rangle = \langle v''w'' \rangle = 0$. Significant cross-plane shear stresses $\langle v''w'' \rangle$ – a component difficult to measure experimentally – are concentrated in small areas, especially near the corners. Unlike the other components, $\langle v''w'' \rangle$, which is closely related to the presence of secondary flow, exhibits a high degree of antisymmetry with respect to the sidewall bisector; this is because $w = 0$ along the top surface, so that both top and bottom walls act as sinks of $\langle v''w'' \rangle$, in agreement with the observation of previous studies of open-channel turbulent flows (Komori *et al.* 1982; Handler *et al.* 1993).

Figures 8 and 9 (in which the corner region is enlarged and the mean secondary streamlines are superposed on the Reynolds-stress contours) show a rapid decrease in the vertical component and an increase in the horizontal components of the turbulence as the free surface is approached; moreover, most of the energy of the

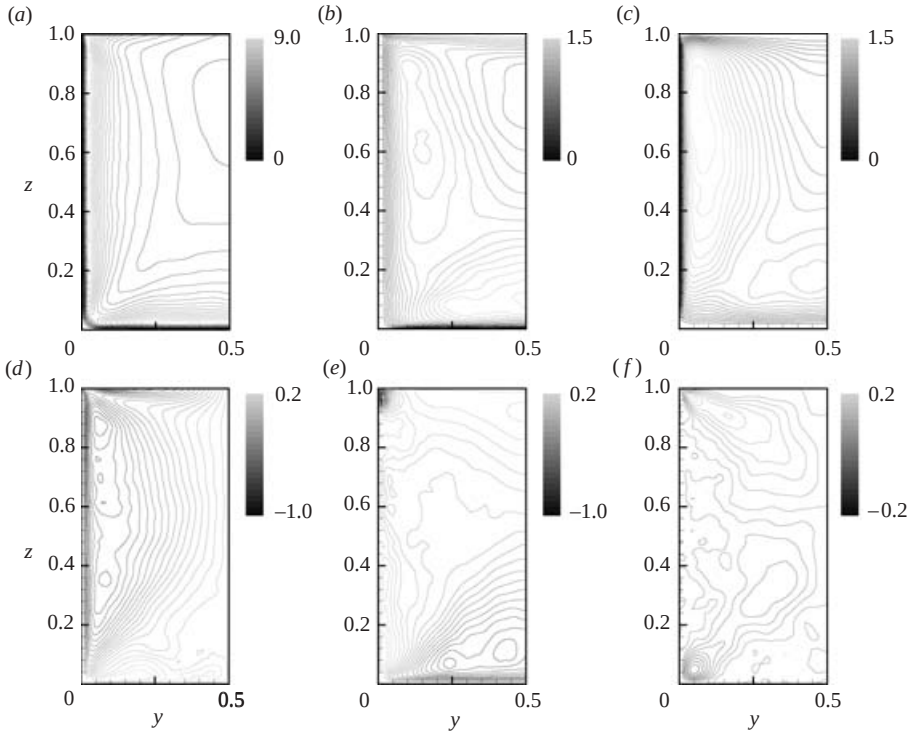

FIGURE 8. Open duct flow, $Re_\tau = 600$: spatial distributions of the resolved Reynolds-stress components. (*a*) $\langle u''u'' \rangle$; (*b*) $\langle v''v'' \rangle$; (*c*) $\langle w''w'' \rangle$; (*d*) $\langle u''v'' \rangle$; (*e*) $\langle u''w'' \rangle$; (*f*) $\langle v''w'' \rangle$.

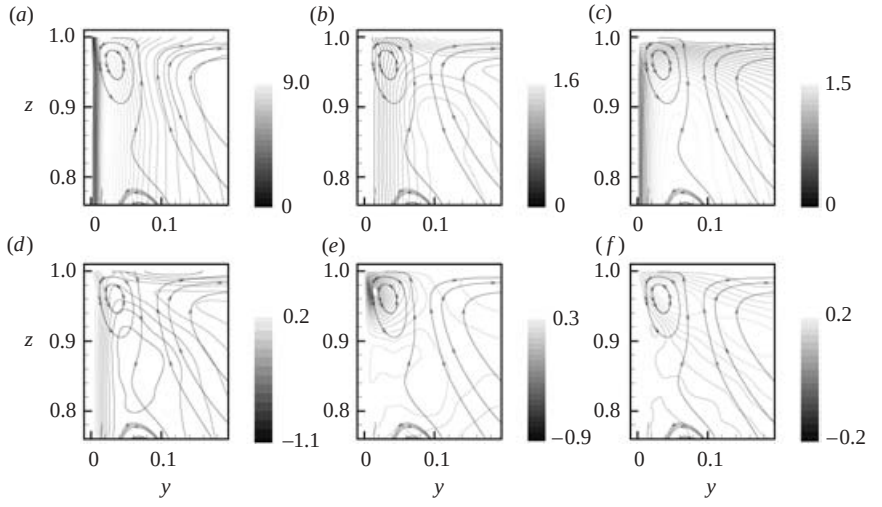

FIGURE 9. Open duct flow, $Re_\tau = 600$: spatial distributions of the resolved Reynolds-stress components near the mixed-boundary corner superposed on the streamlines of the mean secondary flow. (*a*) $\langle u''u'' \rangle$; (*b*) $\langle v''v'' \rangle$; (*c*) $\langle w''w'' \rangle$; (*d*) $\langle u''v'' \rangle$; (*e*) $\langle u''w'' \rangle$; (*f*) $\langle v''w'' \rangle$.

vertical component is transferred to the spanwise component with only a small increase in the streamwise one. The vortical structure plays an important role in decreasing the levels of $\langle w''w'' \rangle$ near the sidewall by convecting fluid from the free surface (where $\langle w''w'' \rangle = 0$) towards the wall. The distributions of $\langle u''v'' \rangle$ and $\langle u''w'' \rangle$

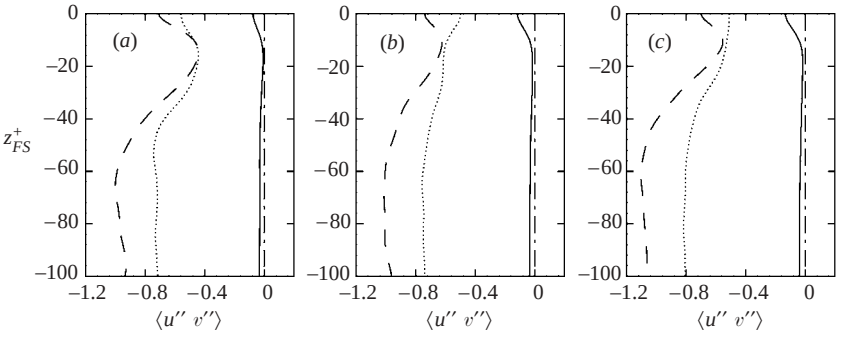

FIGURE 10. Open duct flow: $\langle u''v''\rangle$ Reynolds shear stress. (*a*) $Re_\tau = 360$, (*b*) $Re_\tau = 600$, (*c*) $Re_\tau = 1000$. ——, $y^+ = 3$; · · · · · ·, $y^+ = 15$; – – –, $y^+ = 30$; —·—, $y^+ = Re_\tau/2$.

show the effect of the free surface and the demarcation between inner and outer secondary flows. Near the free surface $-\langle u''v''\rangle$ decreases significantly, with a local maximum at the free surface. This is also shown in figure 10, in which the profiles of $\langle u''v''\rangle$ along constant y-lines are shown; they indicate that, across the interface between inner and outer regions, $\langle u''v''\rangle$ values at the free surface are smaller than those 10–20 viscous lengths away from the free surface. A very strong correlation can be observed between the vortex location and the area in which the secondary shear stress, $\langle u''w''\rangle$, is large. In this region, $\langle u''w''\rangle$ is of the same order of magnitude as $\langle u''v''\rangle$: the turbulent transfer of streamwise momentum in the direction normal to the free-surface is as important as the transport in the wall-normal direction.

Hsu *et al.* (2000) observed an increase in surface-parallel turbulent components for distances from the sidewall greater than 50 viscous lengths, while near the wall all three components of turbulent motion were observed to decrease to a minimum at the free surface. In the present calculation, we also observe that very close to the free surface (within 20 viscous lengths of the free surface) the $\langle u''u''\rangle$ and $\langle v''v''\rangle$ stresses 'rebound' in the near-wall region (figure 11). Outside the inner secondary region ($y^+ \gtrsim 40$), in agreement with the behaviour in open channel flows (Leighton *et al.* 1981; Lam & Banerjee 1992; Handler *et al.* 1993; Pan & Banerjee 1995), the increases in spanwise velocity fluctuations are larger than the increases in the streamwise fluctuations. Figure 11 shows that at the lower wall bisector ($y^+ = Re_\tau/2$), the r.m.s. velocity-fluctuation profiles exhibit trends similar to open channel flows. Indeed, u_{rms} dominates, and near the free surface, turbulence moves towards a quasi-two-dimensional state (see Walker *et al.* 1996). From a mathematical point of view, this behaviour at the centre of the duct is obvious since the Reynolds stresses depend on the shear components, most of which are zero at the centre of the duct since symmetry and fully developed conditions are assumed. A different behaviour was observed at all Reynolds numbers in the region associated with the inner secondary flow: both $\langle u''u''\rangle$ and $\langle v''v''\rangle$ increase near the surface. This issue will be discussed later based on the Reynolds-stress budget data. A difference between the results of the present work and those of Hsu *et al.* (2000) is that the recovery of $\langle u''u''\rangle$ occurs across almost all the surface, except at the lower-wall bisector where $\partial\langle\overline{u}\rangle/\partial y$ is equal to zero and $\partial\langle\overline{u}\rangle/\partial z$ values are almost constant in the region $0.8 < z/D < 1$. Previous studies of Perot & Moin (1995) and Walker *et al.* (1996) revealed significant differences between shear-free boundary layers near solid walls and free surfaces, such as the higher tangential Reynolds stress and lower dissipation near a free surface. Walker

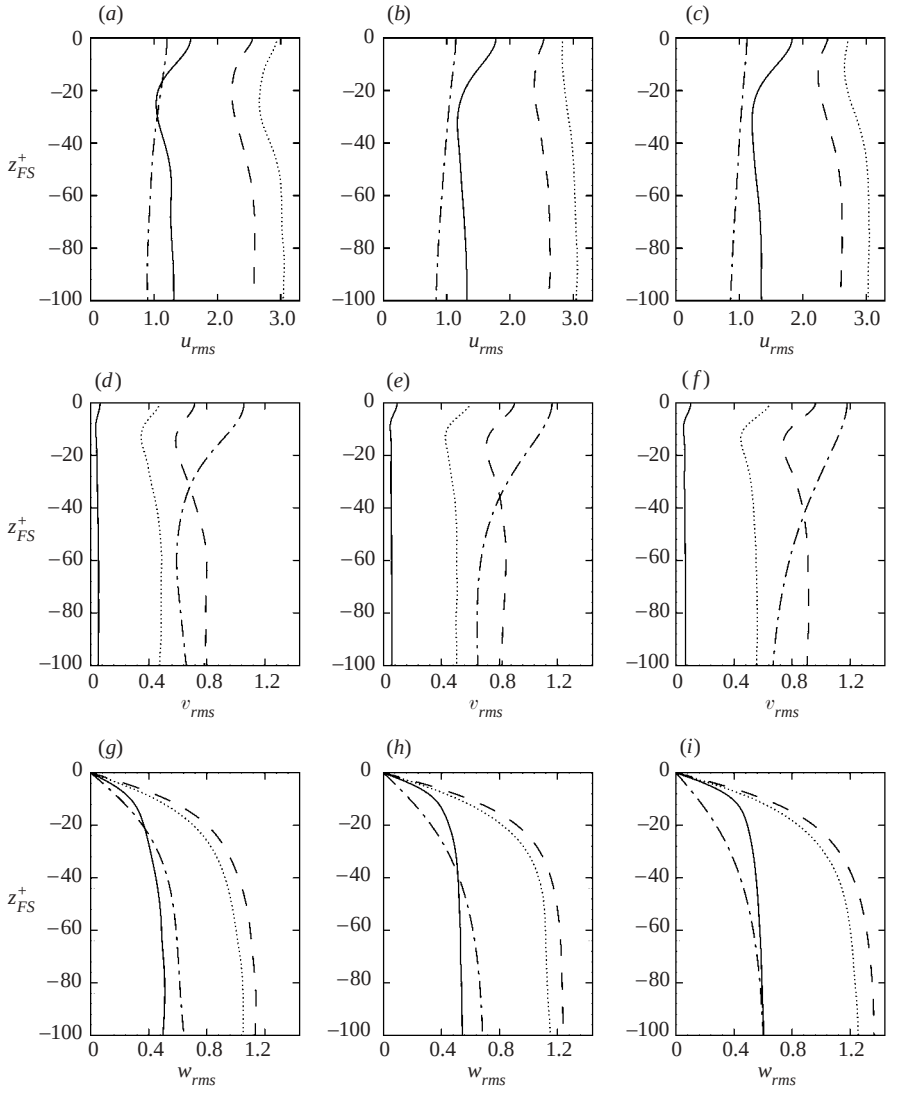

FIGURE 11. Open duct flow: r.m.s. velocity fluctuations normalized with the reference friction velocity. z^+_{FS} is the distance from the free surface in wall units (the reference u_τ is used in this normalization). (*a*)–(*c*) u_{rms}; (*a*) $Re_\tau = 360$, (*b*) $Re_\tau = 600$, (*c*) $Re_\tau = 1000$. (*d*)–(*f*) v_{rms}; (*d*) $Re_\tau = 360$, (*e*) $Re_\tau = 600$, (*f*) $Re_\tau = 1000$. (*g*)–(*i*) w_{rms}; (*g*) $Re_\tau = 360$, (*h*) $Re_\tau = 600$, (*i*) $Re_\tau = 1000$. ——, $y^+ = 3$; ·····, $y^+ = 15$; – – –, $y^+ = 30$; —·—, $y^+ = Re_\tau/2$.

et al. (1996) attribute the apparent increase of turbulence kinetic energy near a rigid-lid boundary to the reduced dissipation of the tangential velocity fluctuations. The persistence of the surface-attached vortices observed in the numerical study of Pan & Banerjee (1995) is also explained by this minimum in dissipation, together with the no-stress boundary conditions. Current calculations indicate that for juncture flows the peculiar production behaviour can affect the velocity fluctuations.

To understand the mechanisms that contribute to the Reynolds stress distributions shown above, we will examine their budgets. The resolved Reynolds-stress transport

equations are of the form:

$$0 = -\langle \overline{u}_k \rangle \frac{\partial \langle u_i'' u_j'' \rangle}{\partial x_k} + \mathscr{P}_{ij} - \epsilon_{ij} + \mathscr{D}_{ij} + \phi_{ij} + \psi_{ij} + \mathscr{T}_{ij}, \tag{3.1}$$

where the terms on the right-hand side represent (rate of) advection, production, dissipation, viscous diffusion, pressure–strain, pressure diffusion, and turbulent diffusion tensors, respectively. The last six terms in (3.1) are defined as:

$$\mathscr{P}_{ij} = -\left[\left(\langle u_j'' u_k'' \rangle \frac{\partial \langle \overline{u}_i \rangle}{\partial x_k} + \langle u_i'' u_k'' \rangle \frac{\partial \langle \overline{u}_j \rangle}{\partial x_k} \right) + \left(\langle \tau_{ik} \rangle \langle \overline{S}_{jk} \rangle + \langle \tau_{jk} \rangle \langle \overline{S}_{ik} \rangle \right) \right], \tag{3.2}$$

$$\epsilon_{ij} = \left[\frac{2}{Re_\tau} \left\langle \frac{\partial u_i''}{\partial x_k} \frac{\partial u_j''}{\partial x_k} \right\rangle - \left(\langle \tau_{ik} \overline{S}_{jk} \rangle + \langle \tau_{jk} \overline{S}_{ik} \rangle \right) \right], \tag{3.3}$$

$$\mathscr{D}_{ij} = \frac{1}{Re_\tau} \frac{\partial^2 \langle u_i'' u_j'' \rangle}{\partial x_k \partial x_k}, \tag{3.4}$$

$$\phi_{ij} = \left\langle p'' \left(\frac{\partial u_i''}{\partial x_j} + \frac{\partial u_j''}{\partial x_i} \right) \right\rangle, \tag{3.5}$$

$$\psi_{ij} = -\frac{\partial}{\partial x_k} \left(\langle p'' u_j'' \rangle \delta_{ik} + \langle p'' u_i'' \rangle \delta_{jk} \right), \tag{3.6}$$

$$\mathscr{T}_{ij} = -\left[\frac{\partial \langle u_i'' u_j'' u_k'' \rangle}{\partial x_k} + \frac{\partial}{\partial x_k} \left(\langle u_j'' \tau_{ik}'' \rangle + \langle u_i'' \tau_{jk}'' \rangle \right) \right]. \tag{3.7}$$

The dissipation and turbulent diffusion consist of two parts: a resolved and a subgrid-scale contribution. To quantify the contribution of the SGS eddies to the terms in the Reynolds-stress budgets, we compare the SGS dissipation $\epsilon_{sgs} = -\langle \tau_{ij} \overline{S}_{ij} \rangle$, the net large-scale energy drained by the subgrid scales, to the total (molecular + SGS) one, ϵ. This is the most significant of the SGS terms that appear in (3.1). The volume-averaged ϵ_{sgs} is 18%, 19% and 21% of the total volume-averaged dissipation, for the three Reynolds numbers considered. Using LES and DNS of mixing layers, Geurts & Fröhlich (2002) found that, when this measure of 'subgrid-activity' is less than 30%, the modelling errors are less than 1%.

Figure 12 shows the terms in the budget of the turbulent kinetic energy $K = \langle u_i'' u_i'' \rangle / 2$. Here and in the following, all terms are normalized by u_τ and ν. Advection is negligible everywhere except in the mixed-boundary corner, as will be discussed later, and is not shown in this figure. Along the side and bottom walls the budget resembles that observed in a flat-plate boundary layer: production and dissipation are nearly in balance, except very near the wall itself, where turbulent and viscous diffusion become important. An enlargement of the corner region, in which the secondary-flow streamlines are superposed on the budget terms and advection is shown in figure 13.

The turbulent kinetic energy is dominated by the streamwise stress $\langle u'' u'' \rangle$, whose production (shown in figure 14*c*) includes the main shear components, $\partial \langle \overline{u} \rangle / \partial y$, $\partial \langle \overline{u} \rangle / \partial z$. The terms in the budgets for the two other normal components (shown in figures 15 and 16, respectively) are smaller than those in the streamwise one by an order of magnitude, reflecting the absence of a significant shear in the production term. All terms contribute to the budgets of $\langle v'' v'' \rangle$ and $\langle w'' w'' \rangle$.

Hsu *et al.* (2000), observed that both TKE production and dissipation are dramatically reduced in the near-corner region, close to the free surface. Far from the wall, this results in an increase of the surface-parallel fluctuations very close to the free surface. Close to the sidewall and within 20 viscous lengths of the free surface, all

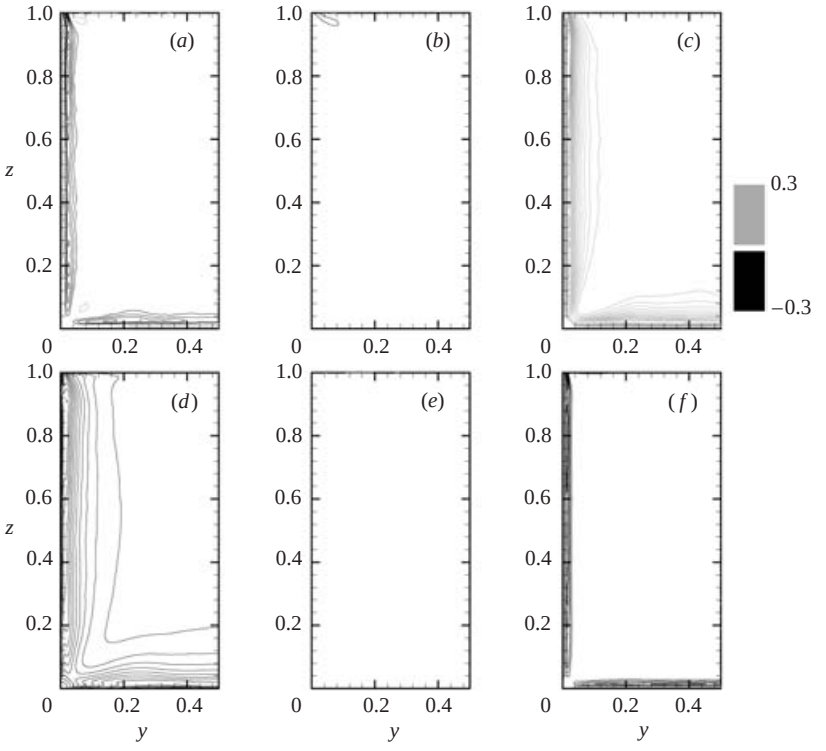

FIGURE 12. Open duct flow, $Re_\tau = 600$: spatial distributions of the terms in the budget of $K = \langle u_i'' u_i'' \rangle / 2$. (*a*) Turbulent diffusion; (*b*) pressure diffusion; (*c*) production; (*d*) dissipation; (*e*) pressure–strain; (*f*) viscous diffusion.

three components of turbulent motions were reported to decrease to a minimum at the free surface. This reduction was explained by Shen *et al.* (1999) through two mechanisms: the annihilation of w'' due to the constraint on the vertical motion at the free surface, and the vanishing of $\partial \langle \overline{u} \rangle / \partial z$ caused by the shear-free boundary condition. Our calculations agree only in part with the experimental findings. While a decrease of the production is observed in the corner region as the free surface is approached, we observe that the production of $\langle u'' u'' \rangle$ increases near the free surface (figure 14*c*), but that of $\langle v'' v'' \rangle$ decreases (figure 15*c*). Near the inner secondary-flow cell, production appears to rebound, and the imbalance between production and dissipation is balanced by advection of TKE away from the corner, along the sidewall. Among the production terms that contribute to the TKE, $-\langle u'' v'' \rangle \partial \langle \overline{u} \rangle / \partial y$ is the dominant one in the corner region.

To complete the above picture, in figure 17 the dependence of the TKE budget terms on the Reynolds number is examined. The distributions of different terms, non-dimensionalized with the reference u_τ and ν, are presented. The corner does not affect the wall scaling expected near a solid boundary for most of the terms (notably production and dissipation, the leading ones in this region). Only advection, which is determined by the interaction between the inner and outer secondary-flow cells, deviates significantly from this scaling.

We will now discuss the budgets of the normal Reynolds stresses in the corner region (figures 14–16) by first describing how the solid-wall/free-surface juncture alters the mechanism of the intercomponent energy transfer. The production rate,

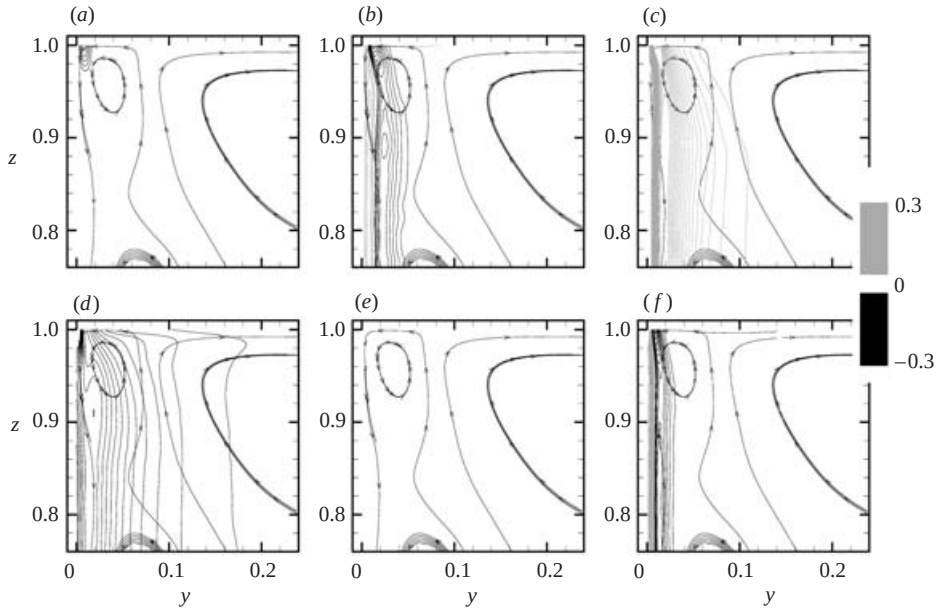

FIGURE 13. Open duct flow, $Re_\tau = 600$: spatial distributions of the terms in the budget of $K = \langle u_i'' u_i'' \rangle / 2$ near the mixed-boundary corner superposed on the streamlines of the mean secondary flow. (*a*) Advection; (*b*) pressure and turbulent diffusion; (*c*) production; (*d*) dissipation; (*e*) pressure–strain; (*f*) viscous diffusion.

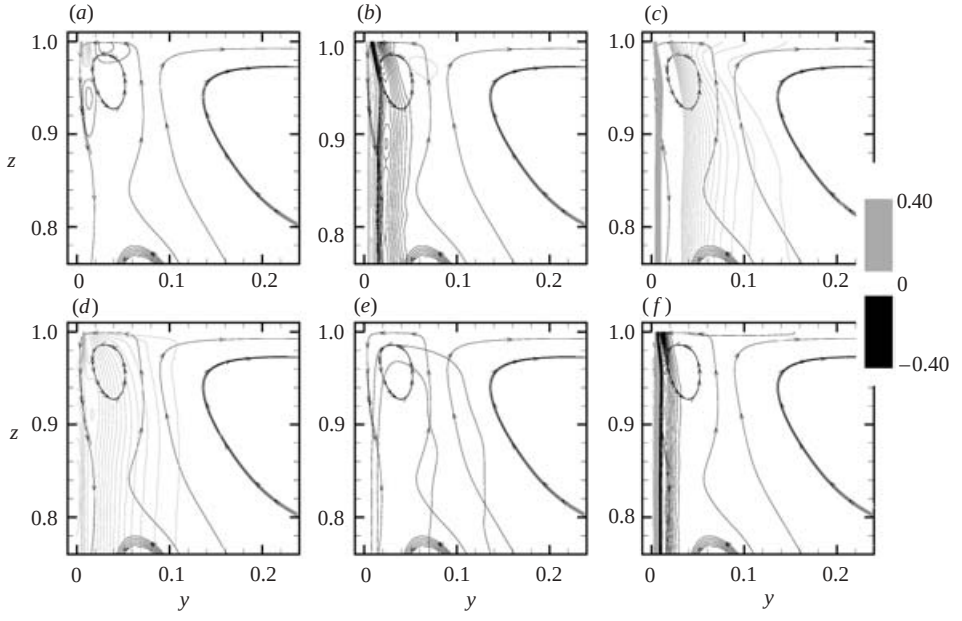

FIGURE 14. Open duct flow, $Re_\tau = 600$: spatial distributions of the terms in the budget of $\langle u'' u'' \rangle$ near the mixed-boundary corner superposed on the streamlines of the mean secondary flow. (*a*) Advection; (*b*) pressure and turbulent diffusion; (*c*) production; (*d*) dissipation; (*e*) pressure–strain; (*f*) viscous diffusion.

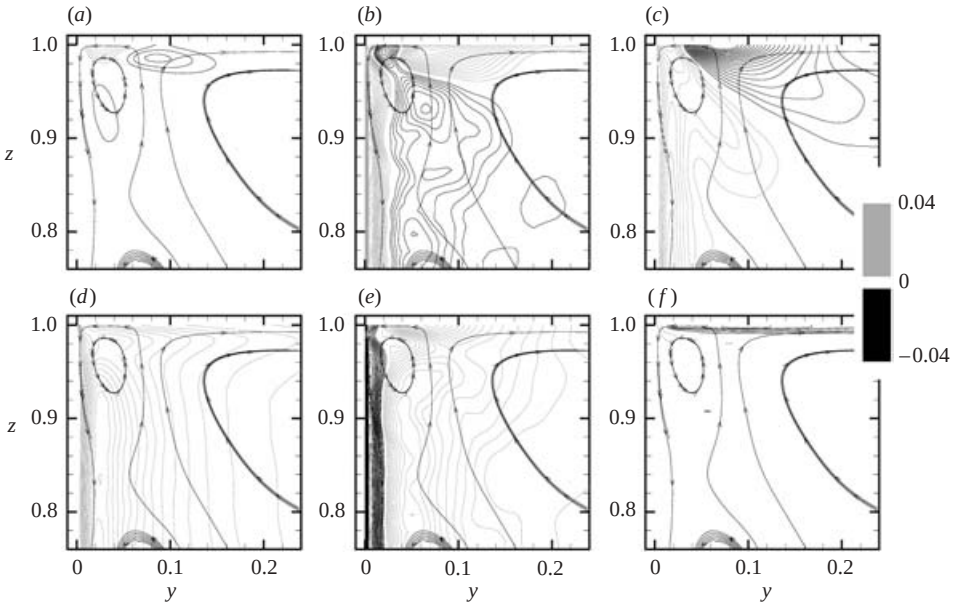

FIGURE 15. Open duct flow, $Re_\tau = 600$: spatial distributions of the terms in the budget of $\langle v''v'' \rangle$ near the mixed-boundary corner superposed on the streamlines of the mean secondary flow. (*a*) Advection; (*b*) pressure and turbulent diffusion; (*c*) production; (*d*) dissipation; (*e*) pressure–strain; (*f*) viscous diffusion.

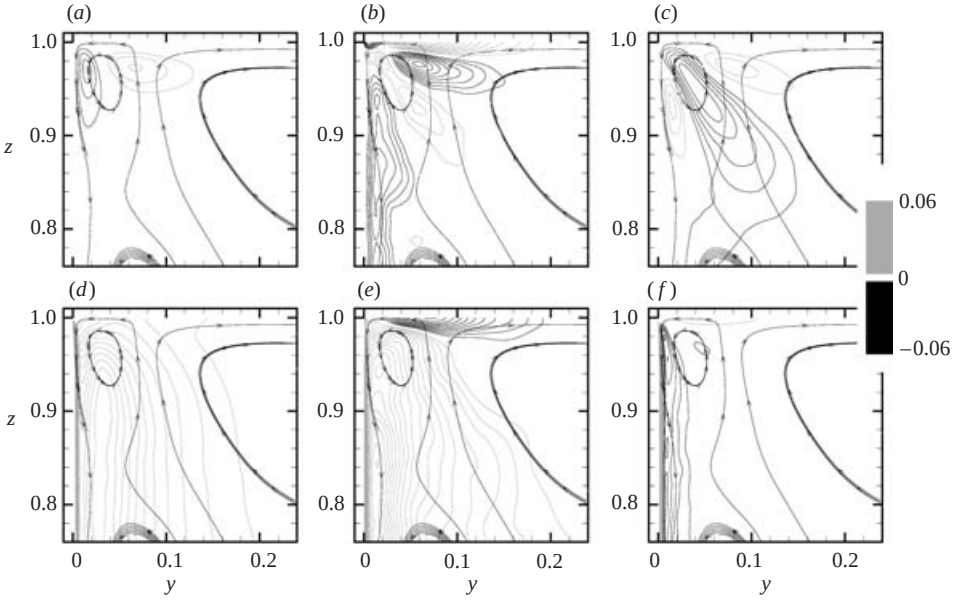

FIGURE 16. Open duct flow, $Re_\tau = 600$: spatial distributions of the terms in the budget of $\langle w''w'' \rangle$ near the mixed-boundary corner superposed on the streamlines of the mean secondary flow. (*a*) Advection; (*b*) pressure and turbulent diffusion; (*c*) production; (*d*) dissipation; (*e*) pressure–strain; (*f*) viscous diffusion.

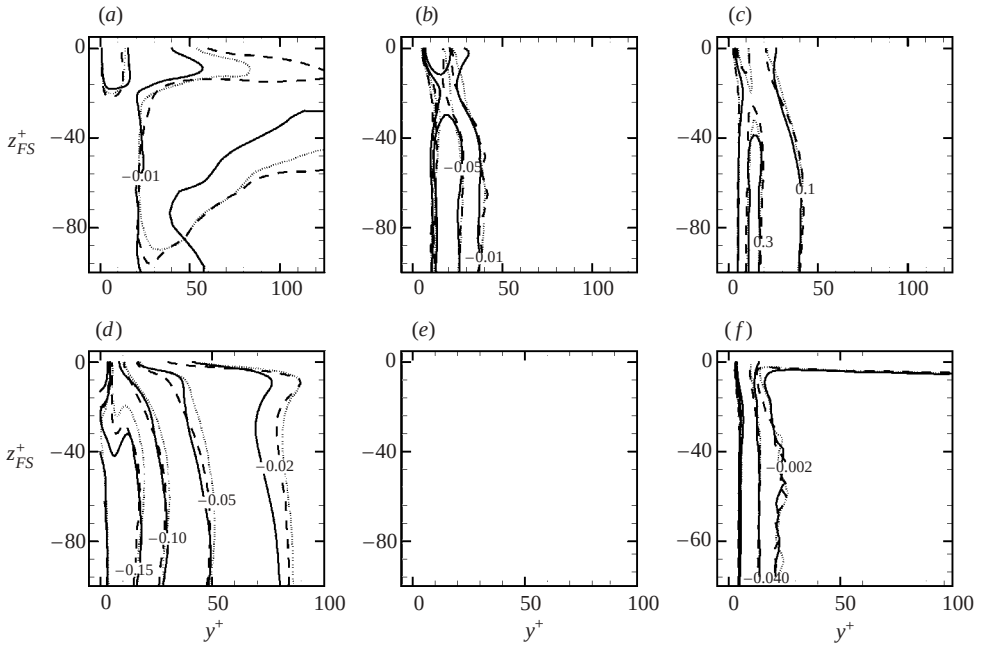

FIGURE 17. Open duct flow, $Re_\tau = 600$: spatial distributions of the terms in the budget of $K = \langle u_i'' u_i'' \rangle / 2$ near the mixed-boundary corner. (*a*) Advection; (*b*) pressure and turbulent diffusion; (*c*) production; (*d*) dissipation; (*e*) pressure–strain; (*f*) viscous diffusion. ——, $Re_\tau = 360$; · · · · · ·, $Re_\tau = 600$; – – –, $Re_\tau = 1000$.

$\mathscr{P}_{33}$, which, together with $\mathscr{P}_{22}$ and $\mathscr{P}_{23}$, contains only secondary shear components (namely, $\partial\langle\overline{v}\rangle/\partial y$, $\partial\langle\overline{v}\rangle/\partial z$, $\partial\langle\overline{w}\rangle/\partial y$ and $\partial\langle\overline{w}\rangle/\partial z$), goes to zero at the free surface and is not directly related to the corresponding Reynolds stress distribution $\langle w''w'' \rangle$ (figures 9*c* and 16*c*). In this region, the distribution of $\langle w''w'' \rangle$ is more influenced by the surface-normal contribution of the pressure–strain, ϕ_{33} (see figure 16*e*).

The 'pressure–rate-of-strain' tensor, ϕ_{ij}, distributes energy among the components of normal stresses $\langle u''u'' \rangle$, $\langle v''v'' \rangle$ and $\langle w''w'' \rangle$, usually shifting energy from the components of the Reynolds stress tensor that receive most of the production by mean shear into the others. Since ϕ_{ij} involves pressure fluctuations, it represents a term associated with non-local interactions and (in wall-bounded flows) is the most important contribution to the pressure correlation tensor $\Pi_{ij} = \phi_{ij} + \psi_{ij}$ in the buffer and the logarithmic region. Near the sidewall ϕ_{ij} and ψ_{ij} are opposite-valued and cancel each other (similarly to what happens in plane channel flow (Mansour, Kim & Moin 1988). Toward the middle plane the distribution of ϕ_{33} is qualitatively different from the results of open-channel flow (Handler *et al.* 1993; Komori *et al.* 1993). In the corner region, up to the demarcation between inner and outer secondary flow, ϕ_{33} decreases and becomes negative as the free surface is approached, whereas it remains positive elsewhere. This indicates that the pressure–strain term, which increases $\langle w''w'' \rangle$ throughout nearly the entire flow region, near the inner secondary-flow region transfers the surface-normal component of TKE to the other components. At the free surface in the outer secondary region, ϕ_{33} is also a production term, but opposite to ψ_{33}; they cancel each other. Apart from a small negative region very near the sidewall, on the other hand, ϕ_{22} remains positive in the boundary layer below the free surface (figure 15*e*), while ϕ_{11}, which is negative throughout nearly

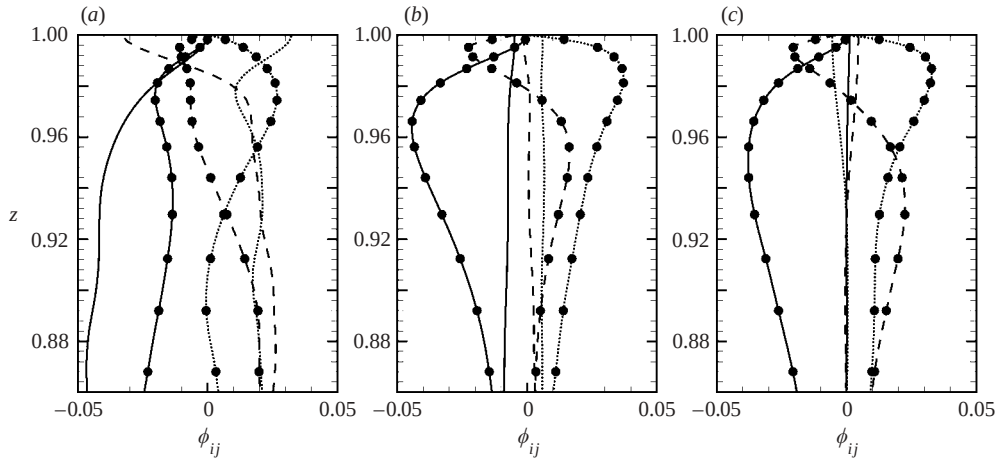

FIGURE 18. Profiles of the diagonal components of the pressure-strain correlation tensor for $Re_\tau = 600$ at different distances from the sidewall: (*a*) $y = 0.065$; (*b*) $y = 0.203$; (*c*) $y = 0.5$. Lines: open duct. Lines and symbols: closed duct. ——, ϕ_{11}; · · · · · ·, ϕ_{22}; – – –, ϕ_{33}.

the entire mixed-corner region, becomes very slightly positive at the free surface (figure 14*e*). Note that $\psi_{11} = 0$, because the flow is homogeneous in the streamwise direction. Noting that $|\phi_{22}| > |\phi_{11}|$ through most of the corner region we conclude that, outside of the inner secondary region, the dominant energy transfer is from the surface-normal component to the spanwise one, in agreement with previous studies of boundary layers adjacent to the free surface (Handler *et al.* 1993; Perot & Moin 1995; Walker *et al.* 1996).

In the inner region, however, a different behaviour can be observed. This is illustrated in figure 18, in which profiles of the diagonal components of the pressure–rate-of-strain tensor, ϕ_{11}, ϕ_{22} and ϕ_{33}, at two y-locations are compared with the corresponding terms from the closed-duct simulation. At $y = 0.065$ (figure 18*a*), ϕ_{33} causes a loss of $\langle w''w'' \rangle$ immediately below the free surface (in the open duct) or the wall (in the closed duct). At the solid–solid corner, we can distinguish two layers: one, next to the solid wall, in which the $\langle w''w'' \rangle$ stress is distributed both to $\langle u''u'' \rangle$ and $\langle v''v'' \rangle$ through a negative ϕ_{33} and increased ϕ_{11} and ϕ_{22}; this is similar to the 'splatting effect' that occurs in the vicinity of a solid boundary (Moin & Kim 1982). For $0.95 < z < 0.98$, however, the decrease of $\langle w''w'' \rangle$ results mostly in an increase of $\langle v''v'' \rangle$; this effect, in which only one Reynolds-stress component is increased, while another is decreased, is called a 'corner effect' by Huser *et al.* (1994). Near the mixed juncture there is little evidence of the corner effect: the spanwise component ϕ_{22} is positive and increases approaching the interface; the streamwise component ϕ_{11} also becomes slightly positive in the vicinity of the free surface. Thus, in this region the vertical component of TKE is distributed both to $\langle u''u'' \rangle$ and $\langle v''v'' \rangle$. Further away from the sidewall, for $y = 0.203$, only the splatting effect is present both in the solid and in the mixed corners.

In the present problem, all the off-diagonal Reynolds stresses are non-zero. Their budgets in the corner region are shown in figures 19–21. The contours of $\langle u''v'' \rangle$ and $\langle u''w'' \rangle$, which are responsible, respectively, for the transport of streamwise momentum in sidewall and free-surface normal directions, are correlated with those of the production terms $\mathscr{P}_{12}$ and $\mathscr{P}_{13}$, in which a connection between primary and secondary shear stresses is present, and the terms containing products of main strain components and normal stresses are dominant. The distribution of $\langle v''v'' \rangle$ mainly affects the

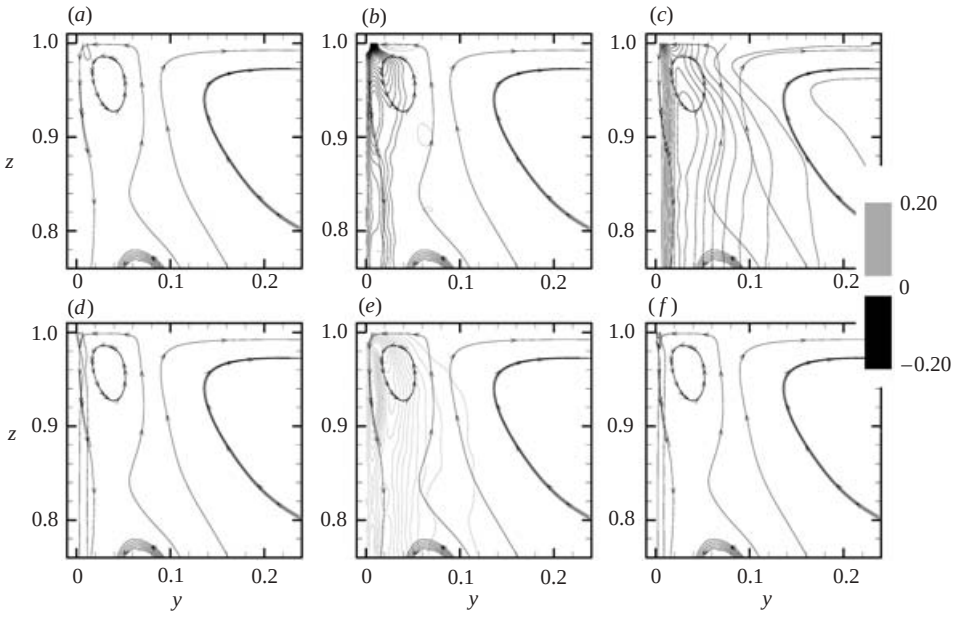

FIGURE 19. Open duct flow, $Re_\tau = 600$: spatial distributions of the terms in the budget of $\langle u''v'' \rangle$ near the mixed-boundary corner superposed on the streamlines of the mean secondary flow. (*a*) Advection; (*b*) pressure and turbulent diffusion; (*c*) production; (*d*) dissipation; (*e*) pressure–strain; (*f*) viscous diffusion.

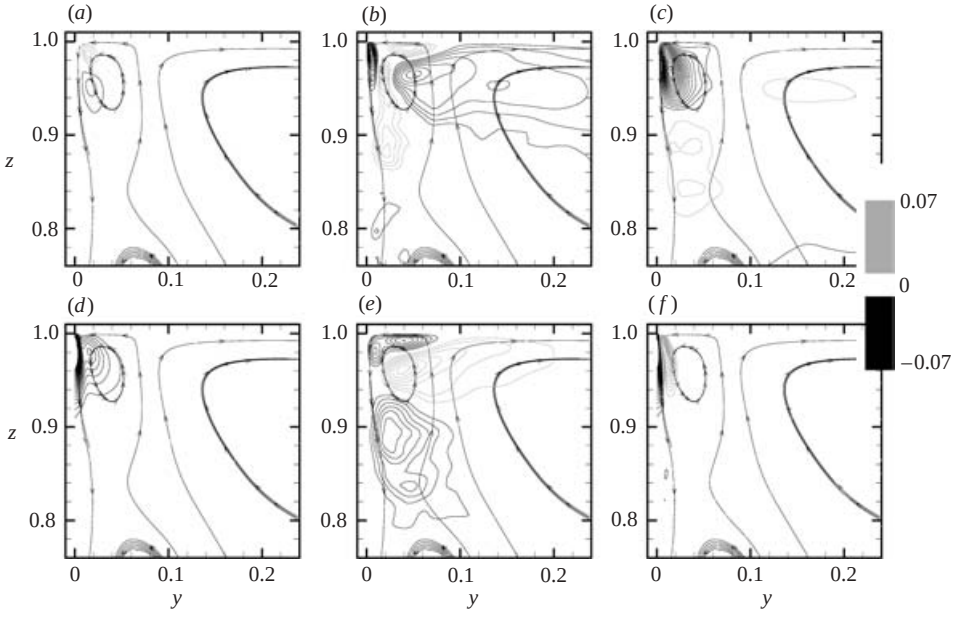

FIGURE 20. Open duct flow, $Re_\tau = 600$: spatial distributions of the terms in the budget of $\langle u''w'' \rangle$ near the mixed-boundary corner superposed on the streamlines of the mean secondary flow. (*a*) Advection; (*b*) pressure and turbulent diffusion; (*c*) production; (*d*) dissipation; (*e*) pressure–strain; (*f*) viscous diffusion.

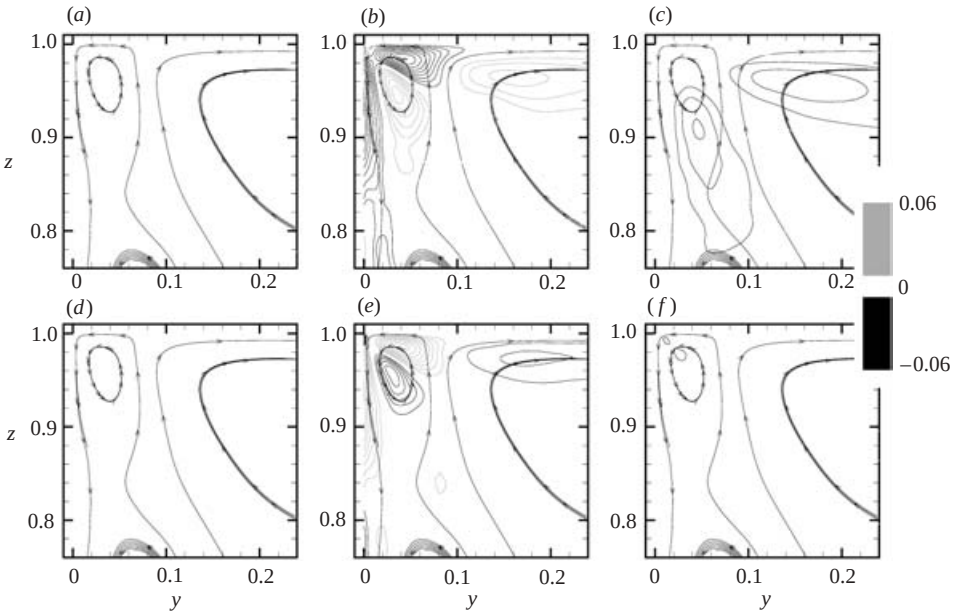

FIGURE 21. Open duct flow, $Re_\tau = 600$: spatial distributions of the terms in the budget of $\langle v''w''\rangle$ near the mixed-boundary corner superposed on the streamlines of the mean secondary flow. (*a*) Advection; (*b*) pressure and turbulent diffusion; (*c*) production; (*d*) dissipation; (*e*) pressure–strain; (*f*) viscous diffusion.

production of $\langle u''v''\rangle$ through $\mathscr{P}_{12} \simeq -\langle v''v''\rangle \partial\langle\overline{u}\rangle/\partial y$, while the variation of $\langle w''w''\rangle$ is a significant mechanism for the $\langle u''w''\rangle$ generation, since $\mathscr{P}_{13} \simeq -\langle w''w''\rangle \partial\langle\overline{u}\rangle/\partial z$. At the mixed corner, $\partial\langle\overline{u}\rangle/\partial y$ monotonically increases approaching the sidewall, but the production of $\langle u''v''\rangle$ shows a small reduction owing to the changes in the distributions of $\langle v''v''\rangle$ in this region along the free surface. The pressure–strain term ϕ_{12} appears as a gain in the $\langle u''v''\rangle$ budget throughout nearly the entire corner region, having a local maximum near the core of the inner cell. The production of $\langle u''w''\rangle$ changes sign at the demarcation between inner and outer secondary flow and becomes negative in regions associated with the inner secondary cell, since $\partial\langle\overline{u}\rangle/\partial z$, zero at the free surface, attains a local maximum immediately below the interface due to the secondary motions. Term ϕ_{13} presents a more complicated pattern. The negative extreme values of $\langle u''v''\rangle$ and $\langle u''w''\rangle$ in the core of the inner secondary region affect directly the production of $\langle u''u''\rangle$, $\mathscr{P}_{11} \simeq -2(\langle u''v''\rangle \partial\langle\overline{u}\rangle/\partial y + \langle u''w''\rangle \partial\langle\overline{u}\rangle/\partial z)$, which increases at the inner secondary flow cell, and remains positive across the surface. As previously stressed, in the central part of the duct $\partial\langle\overline{u}\rangle/\partial y$ goes to zero; this reduces the corresponding term in $\mathscr{P}_{11}$. The remaining term in $\mathscr{P}_{11}$ is also reduced close to the free surface because of the suppression of $\partial\langle\overline{u}\rangle/\partial z$ by the shear-free boundary condition. Furthermore, in the budget for $\langle u''u''\rangle$ the pressure–strain term ϕ_{11} appears as a slightly positive quantity at the free surface (figure 18*c*) and hence it may be thought of as pseudo-production term as far as the streamwise fluctuations are concerned. The gained energy is transported by the diffusion terms and lost by dissipation. In the open-channel flow, the pressure–strain term ϕ_{33} decreases and becomes negative near the surface. The term ϕ_{33} and the dissipation term ϵ_{33} nearly balance across almost the entire depth of the channel, but near the free surface and near the wall ϕ_{33} balances with ψ_{33}, the pressure diffusion term. In the open-channel flow, P_{22} and P_{33} are identically zero, i.e. in the budgets for

$\langle v''v''\rangle$ and $\langle w''w''\rangle$, no direct production term exists. Here, at the lower wall bisector, $\mathscr{P}_{22} \simeq -2\langle v''v''\rangle \partial\langle\overline{v}\rangle/\partial y$ and $\mathscr{P}_{33} \simeq -2\langle w''w''\rangle \partial\langle\overline{w}\rangle/\partial z$. While the latter goes to zero at the interface, the former is a positive quantity. This difference balances with a negative ϕ_{22} (see figure 18*c*). Since $\Pi_{kk} = 0$ from continuity, an increase in ϕ_{22} can be expected to result in a decrease in the magnitude of ϕ_{33}. The budget for $\langle w''w''\rangle$ confirms this line of reasoning. It should be noted here that, as is the case in solid–solid corners (Huser *et al.* 1994), the turbulence dissipation-rate tensor contributes significantly to the Reynolds stress balance, both near the walls and far from them. Figure 20 shows high-dissipation events in the high-turbulence production area.

The cross-plane Reynolds stress, $\langle v''w''\rangle$ (which is identically zero in two-dimensional turbulent shear flows) together with the anisotropy of the normal stresses in the (y, z)-plane, controls the production of the mean streamwise vorticity, whose complete balance is deferred to the next paragraph. In the present configuration, the Reynolds stress production rates that contain the secondary shear stress, $\langle v''w''\rangle$, are weak. Previous studies on three-dimensional duct flows have shown that generation of $\langle v''w''\rangle$ results from two mechanisms, one associated with the gradients of secondary velocities, the other with the distortion of primary velocity gradients (Perkins 1970). The former mechanism seems more effective that the latter (Demuren & Rodi 1984). Along the sidewall there is a positive production of $\langle v''w''\rangle$ caused by the secondary Reynolds stresses; this $\mathscr{P}_{23}$ balances the negative contribution from ϵ_{23}. Along the free surface, on the other hand, the magnitudes of all terms on the right-hand side of the $\langle v''w''\rangle$ balance equation, although small, appear to be of equal magnitude.

3.4. *Open duct: vorticity*

As outlined above, in an open square duct, mean three-dimensionality results in non-zero mean streamwise vorticity $\langle\omega_x\rangle = \partial\langle\overline{w}\rangle/\partial y - \partial\langle\overline{v}\rangle/\partial z$. The origin of the mean secondary flow can be linked to the same mechanisms as those in a closed square duct, since in both cases the anisotropy of the turbulence stress is the driving force that generates the secondary flows. The relationship between the Reynolds-stress anisotropy and the secondary flow is illustrated by the transport equation for $\langle\omega_x\rangle$. In a statistically steady fully developed turbulent flow, in which streamwise gradients are identically zero, the quasi-inviscid stretching and deflection (skew-induced) generation term cancels and this equation reads

$$\underbrace{\langle\overline{v}\rangle\frac{\partial\langle\omega_x\rangle}{\partial y} + \langle\overline{w}\rangle\frac{\partial\langle\omega_x\rangle}{\partial z}}_{\mathrm{I}} \underbrace{- \frac{1}{Re_\tau}\left(\frac{\partial^2\langle\omega_x\rangle}{\partial y^2} + \frac{\partial^2\langle\omega_x\rangle}{\partial z^2}\right)}_{\mathrm{II}}$$
$$\underbrace{- \frac{\partial^2}{\partial y\partial z}\left(\langle v''^2 + \tau_{yy}\rangle - \langle w''^2 + \tau_{zz}\rangle\right)}_{\mathrm{III}} \underbrace{- \left(\frac{\partial^2}{\partial y^2} - \frac{\partial^2}{\partial z^2}\right)\langle v''w'' + \tau_{yz}\rangle}_{\mathrm{IV}} = 0. \quad (3.8)$$

Term I represents advection of the mean streamwise vorticity by mean secondary velocities; term II is the diffusion of vorticity due to viscosity; III and IV are production terms (resolved + SGS) due to the gradient of the difference in the normal Reynolds stresses ($\langle v''^2 + \tau_{yy}\rangle - \langle w''^2 + \tau_{zz}\rangle$), and to the difference in the gradient of the secondary shear Reynolds stress ($\langle v''w'' + \tau_{yz}\rangle$), respectively.

It has been argued by other investigators (see, for example, Perkins 1970) that, for fully developed flows, the imbalance between gradients of normal stresses is primarily responsible for the production of secondary flow vorticity, whereas the shear-stress contribution, if not negligible, acts like a transport term in (3.8). For a more thorough

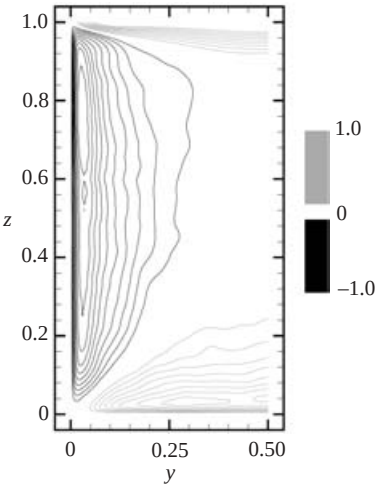

FIGURE 22. Open duct flow, $Re_\tau = 600$: spatial distribution of the resolved anisotropy term ($\langle v''v'' \rangle - \langle w''w'' \rangle$). Twenty-one equispaced contours between ± 1.

discussion of the associated flow phenomena, see Bradshaw (1987). In the present problem, the mean streamwise vorticity is directly tied to the secondary velocities and the main mechanisms acting in (3.8) play a role in the origin of the secondary flows. In the context of vorticity transport, the turbulent secondary-flow generation in the mixed-corner flow presents a totally different spatial distribution from that in the solid–solid corner, because of the significant differences in the distributions and magnitudes of the turbulent stresses.

Figure 22 displays contours of the resolved anisotropy of the normal Reynolds stresses, $\langle v''v'' \rangle - \langle w''w'' \rangle$. Together with the cross-plane resolved Reynolds stress $\langle v''w'' \rangle$ (shown in figure 8*f*), this term contributes to the production and transport of mean streamwise vorticity. The anisotropic term reaches a minimum along the side wall, where the turbulent fluctuations in the direction normal to the sidewall are suppressed by the boundary conditions. At both corners, the contours show two regions of opposite sign, which are ultimately the cause of the generation of $\langle \omega_x \rangle$. The gradient of the anisotropy term near the mixed corner, however, is higher than that at the solid–solid corner.

Figure 23 shows the spatial distributions of the four terms of equation (3.8) for the $Re_\tau = 600$ calculation. The two-dimensional fields of the different terms of (3.8) are superimposed on filled contours of the mean streamwise vorticity. The contribution of the SGS stresses was found to be negligible compared with the leading terms in (3.8). As already pointed out, in the corner formed by the solid wall and the free surface, $\langle \omega_x \rangle$ has positive/negative extreme values in correspondence with the inner/outer secondary flows. In general, advection represents the smallest contribution to the budget (figure 23*a*), attaining both its extrema inside the inner secondary-flow cell. Advection is negative at the juncture, and reaches a positive maximum on the free surface, between the inner and outer secondary-flow cells, with a marginal impact on the local $\langle \omega_x \rangle$ distribution. At the solid–solid corner (not shown), both Reynolds normal and shear stress contributions are of the same order of magnitude, of opposite sign and dominant with respect to advection. At the mixed corner, on the other hand, the normal-stress contribution is dominant among the production terms, and positive peak values of term III are always larger than negative values of term IV. Furthermore,

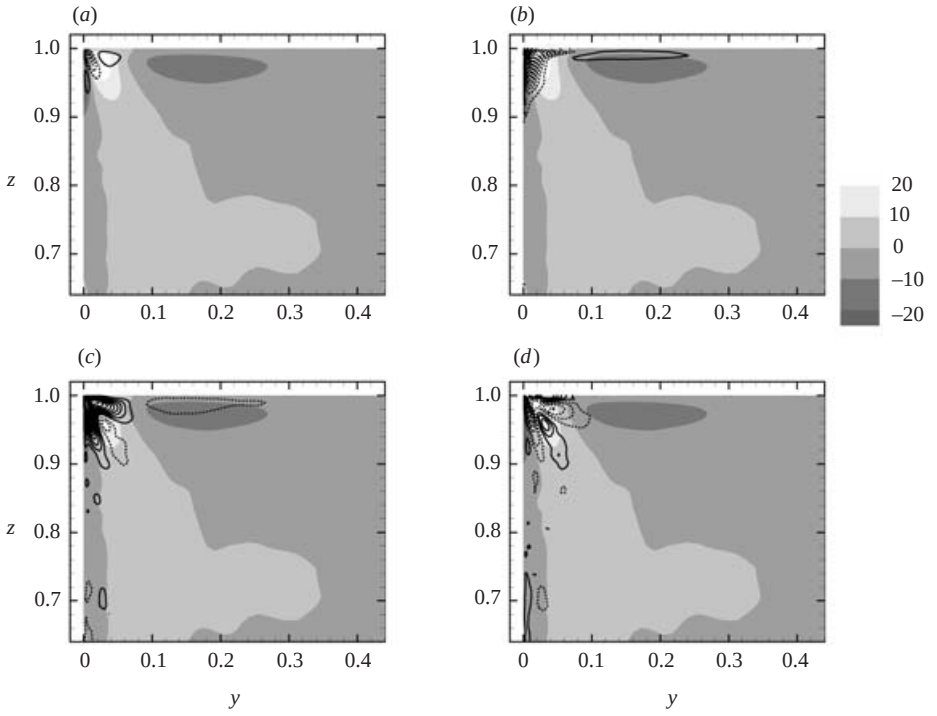

FIGURE 23. Open duct flow, $Re_\tau = 600$. Distributions of the resolved mean streamwise vorticity and terms of the governing balance equation. Contour increments are 100, and dotted lines denote negative contours. (*a*) Advection; (*b*) viscous diffusion; (*c*) production due to normal stress; (*d*) production due to shear stress.

the net positive turbulence contribution overcomes the negative viscous diffusion in the same region, giving rise to a positive streamwise vorticity at the inner secondary flow. As expected, diffusion (figure 23*b*) is significant both close to the corners and very close to the sidewall, but decreases rapidly away from the wall. At the free surface, viscous diffusion acts as a source term in correspondence of the core of the outer secondary flow. At the outer secondary flow, the balance is mainly between terms II and III. The streamwise vorticity distribution along the sidewall, above the viscous sublayer, in the region $0.6 < z/D < 0.9$, is due to the sum of the resolved parts of terms III and IV, which represent the main turbulent contributions to (3.8).

In LES, the vorticity fluctuations are less well-resolved than the velocity fluctuations, since the unresolved scales contribute more to the former than to the latter. In the present calculation, however, the grid resolution is fine enough that even the SGS contribution to the vorticity is fairly small. An indication of this is the observation that the SGS contribution to the total dissipation is between 18% and 21% for all the cases examined. Thus, we believe that at least qualitative conclusions can be drawn by examining the r.m.s. vorticity fluctuations obtained from the present simulation. The surface-parallel components of the r.m.s. vorticity fluctuation, ω_x^{rms} and ω_y^{rms}, decrease inside a very thin layer below the free surface and vanish at the free surface because of the local shear-free condition. The anisotropic vorticity layer is much thinner than the anisotropic velocity layer.

In figure 10, the vertical profiles of the fluctuating velocity components showed the dependence on the Reynolds number of the thickness of the blockage layer. At

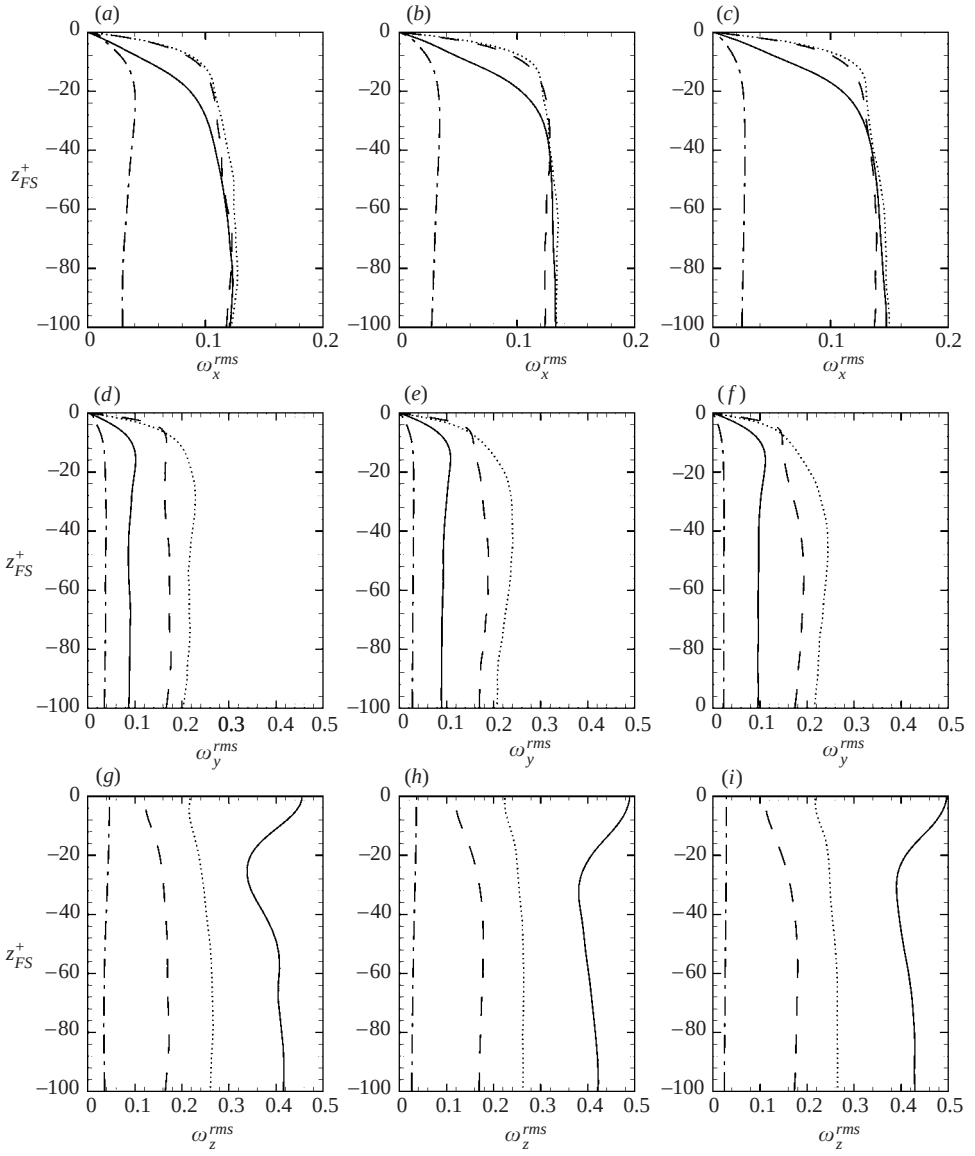

FIGURE 24. Open duct flow: root-mean-square vorticity fluctuations normalized with u_τ^2/ν. z^+_{FS} is the distance from the free surface in wall units (the reference u_τ is used in this normalization). (*a*)–(*c*) ω_x^{rms}; (*a*) $Re_\tau = 360$, (*b*) $Re_\tau = 600$, (*c*) $Re_\tau = 1000$. (*d*)–(*f*) ω_y^{rms}; (*d*) $Re_\tau = 360$, (*e*) $Re_\tau = 600$, (*f*) $Re_\tau = 1000$. (*g*)–(*i*) ω_z^{rms}; (*g*) $Re_\tau = 360$, (*h*) $Re_\tau = 600$, (*i*) $Re_\tau = 1000$. ——, $y^+ = 3$; ·····, $y^+ = 15$; – – – $y^+ = 30$; —·— , $y^+ = Re_\tau/2$.

the bottom-wall bisector, this layer has a thickness of about 40 wall units from the free surface for $Re_\tau = 360$, 60 for $Re_\tau = 600$ and 100 for $Re_\tau = 1000$. In outer coordinates, these vertical positions correspond to $z_{FS} \simeq 0.1$, approximately the same vertical location where the pressure–strain tensor feels the blocking effect of the free surface. Such Reynolds-number dependence is damped out as we move towards the sidewall. On the other hand, the vertical variation of ω_x^{rms}, ω_y^{rms} and ω_z^{rms} in wall variables (figure 24) gives an indication of the thickness of the surface layer, whose

thickness is about 30 wall units and shows only a weak dependence from the sidewall distance. While the streamwise vorticity fluctuations monotonically decrease inside the surface layer to become negligible at the free surface, those normal to the sidewall reach their maxima at $z_{FS}^{+} \simeq 10$ before dropping to zero.

4. Conclusions

Fully developed turbulent open-duct flows at three Reynolds numbers up to $Re_\tau = 1000$ (based on the friction velocity and duct width) was studied by large-eddy simulations. The free surface was approximated by rigid shear-free conditions valid in the zero-limit of Froude and Weber numbers. The mean flow field and a variety of turbulence statistics were studied, to highlight the complex structure of the flow near the mixed corner between the solid wall and the free surface, where the interaction of the wall-bounded turbulence with the free-surface eddies generates complex physical phenomena. In spite of a number of experimental and computational studies of the 'mixed-boundary corner' reported over the past decade, significant differences between investigations result in disagreement on several issues. The present LES contributes to clarify some of these discrepancies.

We find that the effects of the free surface in the square-duct flow produce several substantial changes in the turbulence-driven secondary flows developed near the corners. Here, the maximum value of the cross-stream velocity associated with these secondary flows was found to be about 3% of the bulk velocity, slightly greater than that observed in the companion calculations for closed-duct flows. The main feature of the flow field near to the mixed corner is the existence of an 'inner' counterclockwise and an 'outer' clockwise mean secondary flow. For the three Reynolds numbers considered, the demarcation between inner and outer secondary flows occurs at $\sim$40 viscous lengths from the sidewall while the vertical size of the inner secondary region was found to be $\sim$100 viscous lengths along the sidewall. The scale and the strength of the outer secondary vortex are larger. Furthermore, in contrast to experimental studies, our simulations clearly indicate the formation of a second 'outer' counterclockwise vortical region near the sidewall, directly below the 'inner' one. The effect of the inner secondary motion, which has a parallel in the wall-bounded corner flow, is crucial.

The use of the 'Clauser plot' method to measure the wall stress was found to result in inaccuracies, since the velocity profile near the sidewall deviates significantly from the logarithmic law. Our calculations show that the friction velocity decreases as the free surface is approached, as a result of the outflow region of the inner secondary-flow cell, which thickens the boundary layer and reduces the wall shear stress. Such a behaviour was also documented in previous experimental studies; the present computations, however, also show an increase of u_τ very near the surface, this time owing to the inflow from the inner secondary cell, which convects high-speed momentum toward the sidewall at the free surface. Near the corner, the advection of streamwise momentum due to the secondary motions becomes significant. The present results shed some light on the transverse spreading mechanism of turbulence at the free surface. The two opposite diverging currents generated at the sidewalls and merging at the duct's center have a significant effect on the behaviour of the shear components near the free surface. The multi-layer structure of the boundary-layer near the interface, altered by the secondary motions, shows little dependence on the Reynolds number.

This was the first investigation of 'mixed-boundary corner' flows in which an explanation of the existence and origin of secondary motions could be offered in the context of several balance equations. All of the terms in the streamwise momentum equation, vorticity transport, Reynolds stress budgets and turbulent energy transport were computed from the present LES. Two regions can be distinguished, one in which the advection increases the x-momentum, immediately below the surface, and one further away from the corner, in which the momentum is decreased. The Reynolds-stress gradient adjusts to maintain the balance. The turbulent kinetic energy and Reynolds stress distributions are also significantly affected by the secondary motions in the corner.

Of particular interest are the Reynolds-stress budgets. Two factors play important roles in the Reynolds stress distributions: the pressure–strain redistribution term and the production. Production dominates the budgets whenever the mean shear enters the production term (i.e. for the $\langle u''u''\rangle$, $\langle u''v''\rangle$ and $\langle u''w''\rangle$ components of the Reynolds-stress tensor). The budgets of the other terms are dominated by the pressure–strain term. Outside the inner secondary region, the stress normal to the free surface, $\langle w''w''\rangle$, is transferred mainly to the streamwise one $\langle u''u''\rangle$, in agreement with previous studies of boundary layers adjacent to the free surface. In the inner secondary region, $\langle w''w''\rangle$ is distributed both to $\langle u''u''\rangle$ and $\langle v''v''\rangle$ through the free-surface normal distribution of the pressure–strain term ϕ_{33}. The physical reasons for the TKE increase in the inner region can be summarized as follows: the primary off-diagonal Reynolds stresses, $\langle u''v''\rangle$ and $\langle u''w''\rangle$, fed by $\langle u''u''\rangle$ and $\langle v''v''\rangle$ through the production terms, affect directly the production of $\langle u''u''\rangle$, which increases at the inner secondary flow cell, and remains positive across the surface. At the free surface, as the distance from the sidewall increases, the pressure–strain term ϕ_{33} changes from a destruction to a production term at the demarcation between inner and outer flow regions. The mean secondary motion is driven by the anisotropy of Reynolds stresses; in the mean streamwise vorticity equation, at the mixed corner, the normal-stress contribution is dominant among the production terms. The positive contribution of the turbulence overcomes the negative viscous diffusion in this region, giving rise to positive streamwise vorticity at the inner secondary flow.

The Reynolds-number dependence of the terms in the TKE budget was investigated, and it was found that (within the range of Reynolds numbers examined in this work) the corner does not affect the wall scaling expected near a solid boundary for most of the terms. Only advection deviates significantly from this scaling. While the source-layer thickness is sensitive to the distance from the sidewall, the surface-layer thickness, approximately 30 viscous lengths, is only weakly affected by the wall distance.

Taken together, the results presented in the present paper can contribute to the development of turbulence models for RANS equations, as well as elucidate some important physical mechanisms in this very important configuration. In this regard, this investigation is the precursor of a follow-up flow study in which wave-induced effects are not negligible.

The work of R.B. and A.P. was performed under the auspices of the Italian Ministry of Transportation within the framework of INSEAN Research Plan 2000–02. The computational resources were provided by CINECA (Bologna, Italy) and CASPUR (Roma, Italy). U.P. acknowledges the support of the Office of Naval Research through Grant N000140110993, monitored by Drs L. P. Purtell and R. D. Joslin.

REFERENCES

Akselvoll, K. & Moin, P. 1996 Large-eddy simulation of turbulent confined coannular jets. *J. Fluid Mech.* **315**, 387–411.

Anthony, D. G. & Willmarth, W. W. 1992 Turbulence measurements in a round jet near a free surface. *J. Fluid Mech.* **243**, 699–720.

Borue, V., Orszag, S. & Staroselsky, S. A. 1995 Interaction of surface waves with turbulence: direct numerical simulations of turbulent open-channel flow. *J. Fluid Mech.* **286**, 1–23.

Bradshaw, P. 1987 Turbulent secondary flows. *Annu. Rev. Fluid Mech.* **19**, 53–74.

Broglia, R., Di Mascio, A. & Muscari, R. 1999 Numerical simulations of turbulent flows with a free-surface. In *Proc. 7th Intl Conf. on Numerical Ship Hydrodynamics*, pp. 2.2.1–2.2.7, Nantes, France, 19–22 July.

Chorin, A. J. 1967 A numerical method for solving incompressible viscous flow problems. *J. Comput. Phys.* **2**, 12–26.

Demuren, A. O. & Rodi, W. 1984 Calculation of turbulence-driven secondary motion in non-circular ducts. *J. Fluid Mech.* **140**, 189–222.

Gavrilakis, S. 1992 Numerical simulation of low-Reynolds-number turbulent flow through a straight square duct. *J. Fluid Mech.* **244**, 101–129.

Germano, M., Piomelli, U., Moin, P. & Cabot, W. H. 1991 A dynamic subgrid-scale eddy-viscosity model. *Phys. Fluids* A **3**, 1760–1765.

Gessner, F. B., Po, J. K. & Emery, A. F. 1979 Measurements of developing turbulent flow in a square duct. In *Turbulent Shear Flows I* (ed. F. Durst, B. E. Lavender, F. W. Schmidt, & J. H. Whitelaw). Springer.

Geurts, B. & Fröhlich, J. 2002 A framework for predicting accuracy limitations in large-eddy simulation. *Phys. Fluids* **14**, L41–L44.

Grega, L. M., Hsu, T. Y. & Wei, T. 2002 Vorticity transport in a corner formed by a solid wall and a free surface. *J. Fluid Mech.* **465**, 331–352.

Grega, L. M., Wey, T., Leighton, R. I. & Neves, J. C. 1995 Turbulent mixed-boundary flow in a corner formed by a solid wall and a free-surface. *J. Fluid Mech.* **294**, 17–46.

Handler, R. A., Swean, T. F., Leighton, R. I. & Swearingen, J. D. 1993 Length scales and the energy balance for turbulence near a free surface. *AIAA J.* **31**, 1998–2007.

Hong, W. L. & Walker, D. T. 2000 Reynolds-averaged equations for free-surface flows with application to high-Froude-number jet spreading. *J. Fluid Mech.* **417**, 183–209.

Hsu, T. Y., Grega, L. M., Leighton, R. I. & Wei, T. 2000 Turbulent kinetic energy transport in a corner formed by a solid wall and a free-surface. *J. Fluid Mech.* **410**, 343–366.

Hunt, J. C. R. & Graham, J. M. R. 1978 Free stream turbulence near plane boundaries. *J. Fluid Mech.* **84**, 209–235.

Huser, A. & Biringen, S. 1993 Direct numerical simulation of turbulent flow in a square duct. *J. Fluid Mech.* **257**, 65–95.

Huser, A., Biringen, S. & Hatay, F. F. 1994 Direct simulation of turbulent flow in a square duct: Reynolds-stress budgets. *Phys. Fluids* **6**, 3144–3152.

Kim, J. & Moin, P. 1985 Application of a fractional-step method to incompressible Navier–Stokes equations. *J. Comput. Phys.* **59**, 308–323

Komori, S., Nagaosa, N., Murakami, Y., Chiba, S., Ishii, K. & Kuwahara, K. 1993 Direct numerical simulation of three-dimensional open-channel flow with zero-shear gas–liquid interface. *Phys. Fluids* A **5**, 115–125.

Komori, S., Ueda, H., Ogino, F. & Mizushina, T. 1982 Turbulent structure and transport mechanism at the free-surface in an open-channel flow. *Intl J. Heat Mass Transfer* **25**, 513–521.

Kumar, S., Gupta, R. & Banerjee, S. 1998 An experimental investigation on the characteristics of free-surface turbulence in channel flow. *Phys. Fluids* **10**, 437–456.

Lam, K. & Banerjee, S. 1992 On the condition of streak formation in a bounded turbulent flow. *Phys. Fluids* A **4**, 306–320.

Launder, B. E. & Ying, W. G. 1972 Secondary flows in ducts of square cross-section. *J. Fluid Mech.* **54**, 289–295.

Leighton, R. I., Swean, T. F., Handler, R. A. & Swearingen, J. D. 1981 Interaction of vorticity with a free-surface in turbulent open-channel flow. *AIAA Paper* 91–0236.

LILLY, D. K. 1992 A proposed modification of the Germano subgrid-scale closure method. *Phys. Fluids* A **4**, 633–635.

LONGO, J., HUANG, H. P. & STERN, F. 1998 Solid/free-surface juncture boundary layer and wake. *Exps. Fluids* **25**, 283–297.

MADABHUSHI, R. K. & VANKA, S. P. 1991 Large eddy simulation of turbulence-driven secondary flow in a square duct. *Phys. Fluids* A **3**, 2734–2745.

MANSOUR, N. N., KIM, J. & MOIN, P. 1988 Reynolds-stress and dissipation rate budgets in a turbulent channel flow. *J. Fluid Mech.* **194**, 15–44.

MELLING, A. & WHITELAW, J. H. 1976 Turbulent flow in a rectangular duct. *J. Fluid Mech.* **78**, 289–315.

MITTAL, R. & MOIN, P. 1997 Suitability of upwind biased schemes for large-eddy simulation of turbulent flows. *AIAA J.* **35**, 1415–1417.

MOIN, P. & KIM, J. 1982 Numerical investigation of turbulent channel flow. *J. Fluid Mech.* **118**, 341–378.

NAKAGAWA, H. & NEZU, I. 1981 Structure of space–time correlations of bursting phenomena in an open-channel flow. *J. Fluid Mech.* **104**, 1–43.

NAGAOSA, R. 1999 Direct numerical simulation of the vortex structures and turbulent scalar transfer across a free surface in a fully developed turbulence. *Phys. Fluids* **11**, 1581–1595.

NEZU, I. & RODI, W. 1986 Open-channel flow measurements with a laser Doppler anemometer. *J. Hydraul. Engng ASCE* **112**, 335–355.

PAN, Y. & BANERJEE, S. 1995 A numerical study of free-surface turbulence in channel flow. *Phys. Fluids* **7**, 1649–1664.

PERKINS, H. J. 1970 The formation of streamwise vorticity in turbulent flow. *J. Fluid Mech.* **44**, 721–740.

PEROT, B. & MOIN, P. 1995 Shear-free turbulent boundary layers. Part 1. Physical insight into near-wall turbulence. *J. Fluid Mech.* **295**, 199–227.

POPE, S. 2000 *Turbulent Flows*. Cambridge University Press.

ROBINSON, S. K. 1991 Coherent motions in the turbulent boundary layer. *Annu. Rev. Fluid Mech.* **23**, 601–640.

SARPKAYA, T. & NEUBERT, D. 1994 Interaction of a streamwise vortex with a free surface. *AIAA J.* **32**, 594–600.

SARPKAYA, T. & SUTHON, P. 1991 Interaction of a vortex couple with a free surface. *Exps. Fluids* **11**, 205–217.

SHEN, L., TRIANTAFYLLOU, G. S. & YUE, D. K. 2000 Turbulent diffusion near a free surface. *J. Fluid Mech.* **407**, 145–166.

SHEN, L., ZHANG, X., YUE, D. K. & TRIANTAFYLLOU, G. S. 1999 The surface layer for free-surface turbulent flows. *J. Fluid Mech.* **386**, 167–212.

SREEDHAR, M. & STERN, F. 1998 Large eddy simulation of temporally developing juncture floes. *Intl J. Numer. Meth. Fluids* **28**, 47–72.

STERN, F., PARTHASARATHY, R., HUANG, H. P. & LONGO, J. 1995 Effects of waves and free surface turbulence in the boundary layer of a surface-piercing flat plate. In *Proc. ASME Fluids Engng Conf. Symp. on Free-Surface Turbulence* (ed. E. Rood & J. Katz). ASME, New York.

SU, M. D. & FRIEDRICH, R. 1994 Investigation of fully developed turbulent flow in a straight duct with large eddy simulation. *J. Fluid. Engng* **116**, 677–684.

TSAI, W. T. 1998 A numerical study of the evolution and structure of a turbulent shear layer under a free surface. *J. Fluid Mech.* **354**, 239–276.

WALKER, D. T. 1997 On the origin of the 'surface current' in turbulent free-surface flows. *J. Fluid Mech.* **339**, 275–285.

WALKER, D. T., LEIGHTON, R. I. & GARZA-RIOS, L. O. 1996 Shear-free turbulence near a solid flat free-surface. *J. Fluid Mech.* **320**, 19–51.